Lower hybrid drift waves during guide field reconnection

Jongsoo Yoo[1], Jeong-Young Ji[2], Manfred V. Ambat[3], Shan Wang[4], Hantao Ji[5], Jenson Lo[6], Bowen Li[7], Yang Ren[5], Jonathan Jara-almonte[1], Li-Jen Chen[8], William Fox[1], Masaaki Yamada[6], Andrew Alt[9], and Aaron Goodman[9]

[1]Princeton Plasma Physics Laboratory (DOE)
[2]Utah State University
[3]University of Rochester
[4]University of Maryland, College Park
[5]PPPL
[6]Princeton University
[7]Department of Physics, Harbin Institute of Technology
[8]NASA Goddard Space Flight Center
[9]Princeton Plasma Physics Laboratory

November 26, 2022

Abstract

Generation and propagation of lower hybrid drift wave (LHDW) within and near the electron diffusion region (EDR) during guide field reconnection at the magnetopause is studied with data from the Magnetospheric Multiscale mission and a theoretical model. Inside the EDR where the electron beta is high (β ˜ 5), the long-wavelength electromagnetic LHDW propagating obliquely to the local magnetic field is observed. In contrast, the short-wavelength electrostatic LHDW propagating nearly perpendicular to the local magnetic field is observed slightly away from the EDR, where β is small (˜0.6). These observed LHDW features are explained by a local theoretical model only after including effects from the electron temperature anisotropy, finite electron heat flux and parallel current. The short-wavelength LHDW is capable of generating significant drag force between electrons and ions.

Lower hybrid drift waves during guide field reconnection

Jongsoo Yoo[1], Jeong-Young Ji[2], M. V. Ambat[3], Shan Wang[4], Hantao Ji[5], Jensen Lo[5], Bowen Li[6], Yang Ren[1], J. Jara-Almonte[1], Li-Jen Chen[4], William Fox[1], Masaaki Yamada[1], Andrew Alt[1], Aaron Goodman[1]

[1]Princeton Plasma Physics Laboratory, Princeton, New Jersey 08543, USA.
[2]Department of Physics, Utah State University, Logan, Utah 84322, USA.
[3]Department of Mechanical Engineering, University of Rochester, Rochester, NY 14627, USA.
[4]NASA Goddard Space Flight Center, Greenbelt, Maryland 20771, USA.
[5]Department of Astrophysical Sciences, Princeton University, Princeton, NJ 08544, USA.
[6]Harbin Institute of Technology, Harbin, China.

Key Points:

- The short-wavelength lower hybrid wave is observed inside a current sheet during guide field reconnection.
- Theoretical model for the dispersion relation of the lower hybrid wave based on local geometry is developed.
- Free energy source for the lower hybrid wave is the perpendicular current and high beta stabilizes the wave.

Corresponding author: Jongsoo Yoo, `jyoo@pppl.gov`

Abstract

Generation and propagation of lower hybrid drift wave (LHDW) within and near the electron diffusion region (EDR) during guide field reconnection at the magnetopause is studied with data from the Magnetospheric Multiscale mission and a theoretical model. Inside the EDR where the electron beta is high ($\beta_{\mathrm{e}} \sim 5$), the long-wavelength electromagnetic LHDW propagating obliquely to the local magnetic field is observed. In contrast, the short-wavelength electrostatic LHDW propagating nearly perpendicular to the local magnetic field is observed slightly away from the EDR, where β_{e} is small (~ 0.6). These observed LHDW features are explained by a local theoretical model only after including effects from the electron temperature anisotropy, finite electron heat flux and parallel current. The short-wavelength LHDW is capable of generating significant drag force between electrons and ions.

1 Introduction

Magnetic reconnection (Yamada, Kulsrud, & Ji, 2010) rapidly releases magnetic energy through topological rearrangement of magnetic field lines. In the diffusion region where reconnection occurs, there are various free energy sources for waves and instabilities. In particular, the lower hybrid drift wave (LHDW) has been observed frequently near the diffusion region in both laboratory (e.g. Carter, Ji, Trintchouk, Yamada, & Kulsrud, 2001; H. Ji et al., 2004; Yoo, Yamada, Ji, Jara-Almonte, Myers, & Chen, 2014) and space (e.g. Chen et al., 2019; Graham et al., 2017; Norgren, Vaivads, Khotyaintsev, & André, 2012). The fast-growing, short-wavelength ($k\rho_{\mathrm{e}} \sim 1$; k is the magnitude of the wave vector $\mathbf{k}$; ρ_{e} is the electron gyroradius), electrostatic LHDW propagating nearly perpendicular to the local magnetic field ($\mathbf{B}_0$) does not exist near the electron diffusion region (EDR) during antiparallel reconnection (Carter et al., 2001; Roytershteyn, Daughton, Karimabadi, & Mozer, 2012; Roytershteyn et al., 2013) due to the stabilization by the high plasma beta (β) (Davidson, Gladd, Wu, & Huba, 1977). The long-wavelength ($k\sqrt{\rho_{\mathrm{e}}\rho_{\mathrm{i}}} \sim 1$; ρ_{i} is the ion gyroradius) electromagnetic LHDW propagating obliquely to $\mathbf{B}_0$ is observed in the EDR (H. Ji et al., 2004; Roytershteyn et al., 2012) but it does not play an important role in fast reconnection under typical magnetosphere conditions (Roytershteyn et al., 2012).

In general, reconnection occurs with guide field, which is a relatively uniform out-of-plane magnetic field component. The presence of the guide field impacts the structure of the diffusion region and electron and ion dynamics (Fox et al., 2017; Pritchett & Coroniti, 2004; Ricci, Blackbill, Daughton, & Lapenta, 2004; Tharp et al., 2012). Moreover, the guide field can reduce β in the EDR, such that the fast-growing, short-wavelength LHDW can exist in the EDR, potentially impacting on reconnection and electron dynamics.

Here we demonstrate that the short-wavelength LHDW is generated near the EDR by analyzing data from the Magnetospheric Multiscale (MMS) mission. In this event, there is a moderate guide field ($B_{\rm g} \sim 0.5 B_{\rm rec}$; $B_{\rm g}$ is the guide field magnitude; $B_{\rm rec}$ is the reconnecting field magnitude). Inside the EDR where $\beta_{\rm e}$ is high (~ 5), the long-wavelength LHDW is present, while the short-wavelength LHDW is excited slightly away from the EDR where $\beta_{\rm e}$ is about 0.6.

Observed LHDW activity are explained by a local theoretical model, improved from a previous model (H. Ji, Kulsrud, Fox, & Yamada, 2005) by including important effects from the electron temperature anisotropy, finite electron heat flux for the parallel temperature, and parallel electron flow. This model address LHDW with an arbitrary angle between $\mathbf{k}$ and $\mathbf{B}_0$ unlike the classical formulation (Davidson et al., 1977). Results from the model agree with measured characteristics of the short-wavelength LHDW; $\mathbf{k}$ is nearly perpendicular to $\mathbf{B}_0$ at $k\rho_{\rm e} \sim 0.7$. The short-wavelength LHDW produces significant drag force between electrons and ions. This study proves that the short-wavelength LHDW can be excited within the EDR under a sufficiently large guide field, potentially affecting electron and reconnection dynamics.

2 Overview of the MMS Event with LHDW

An overview of a magnetopause event observed by MMS2 on December 14, 2015 (Chen et al., 2017; Ergun et al., 2017) is shown in Fig. 1. Here we use burst-mode data from the Fluxgate Magnetometer (FGM) (Russell et al., 2016), Search Coil Magnetometer (SCM) (Le Contel et al., 2016), the electric field spin plane (Lindqvist et al., 2016), axial double probes (Ergun et al., 2016), and Fast Plasma Investigation (FPI) (Pollock et al., 2016). Two magenta vertical lines denote two regions, where the local dispersion relation for LHDW is calculated. The region A represents the EDR (Chen et al., 2017; Ergun et al., 2017), while B is slightly outside the EDR.

The magnetic field profile measured by FGM is shown in Fig. 1(a). The transformation matrix from the geocentric solar ecliptic coordinate to the local LMN coordi-

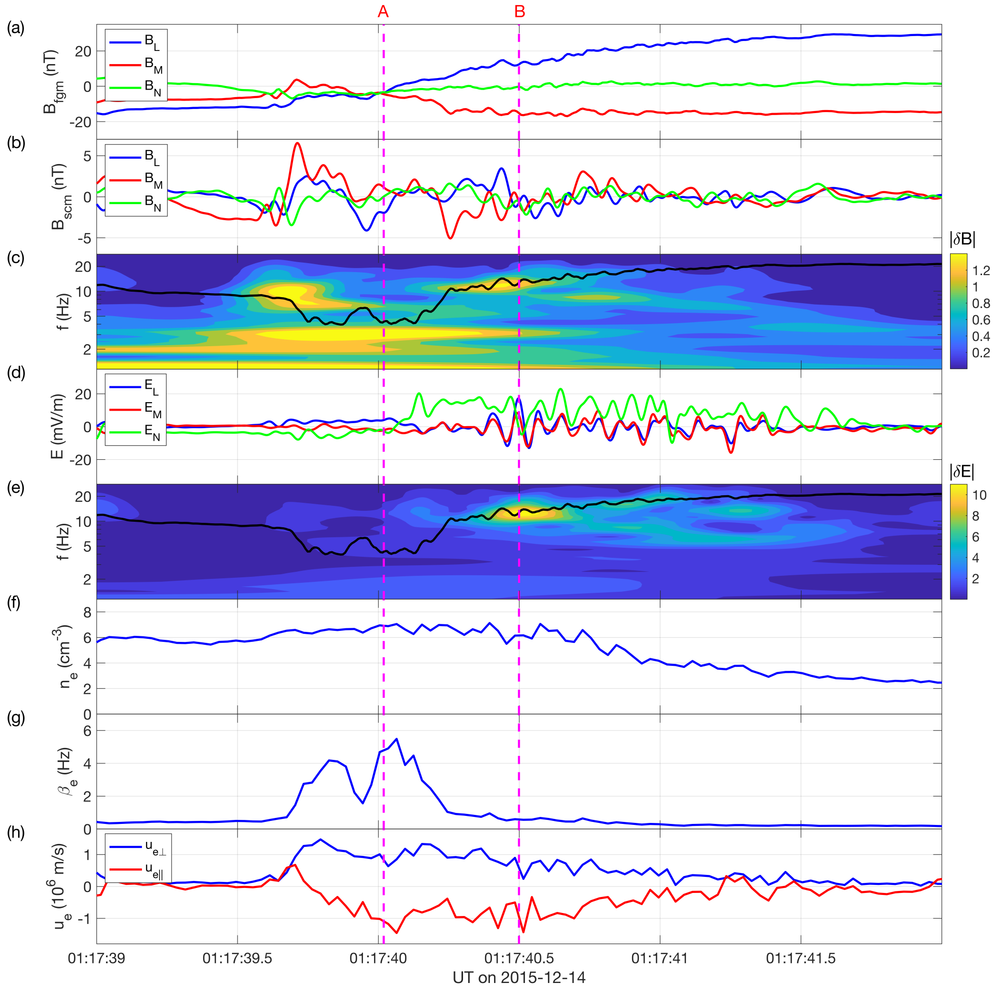

Figure 1. Overview of a magnetopause event with LHDW activity observed by MMS2. Two magenta dashed lines denoted by A and B indicate the time where LHDW stability analysis is performed. The region A represents the EDR, while the region B is slightly outside the EDR. (a) Magnetic field profile measured by FGM. Across the current sheet, there is an average negative B_M component. (b) Magnetic field profile measured by SCM, filtered by a low-pass filter with a cutoff frequency of 40 Hz. (c) Magnetic field spectrogram by the Morlet wavelet. The black line indicates $f_{\rm LH}$. Fluctuations in the magnetic field persists throughout the current sheet crossing (01:17:39.7 – 01:17:41.5). In the region A, the fluctuations is below $f_{\rm LH}$. (d) Electric field profile filtered by the same filter. There are strong fluctuations around the region B. (e) Electric field spectrogram by the wavelet analysis, which demonstrates fluctuations near $f_{\rm LH}$ around the region B. (f) Electron density profile. Density fluctuations exist near B. (g) Profile of $\beta_{\rm e}$. In the region A, $\beta_{\rm e}$ is high, while it becomes small around the region B. (h) Profile of the electron flow. Both parallel (red) and perpendicular (blue) components exist throughout the current sheet crossing.

nate system is $(L, M, N) = ([0.095, -0.481, 0.865], [-0.445, -0.811, -0.392], [0.889, -0.346, -0.290])$, which is obtained by a hybrid method (Yoo & Yamada, 2012) using both the minimum variance analysis and timing analysis, particularly with the assumption of the constant thickness (Haaland et al., 2004). The current sheet thickness for this event is about 130 km, which is larger than the ion skin depth $d_{\rm i}$ in the region B ($\sim$ 90 km). The region A is close to the reversal of the reconnecting field component B_L, while the region B is shifted to the low-density side. Note that there is a density asymmetry across the current sheet with a ratio of about 3, as shown in Fig. 1(f). Profiles of B_L and the electron flow $\mathbf{u}_{\rm e}$ in Fig. 1(h) suggest that MMS2 passes through the current sheet from 01:17:39.7 to 01:17:41.5.

The out-of-plane magnetic field component B_M has a negative value on average, indicating there is a guide field for this event. The large perturbation of B_M from 01:17:39.7 to 01:17:40.3 in Fig. 1(a) is due to the bipolar Hall field structure in asymmetric reconnection (Mozer, Angelopoulos, Bonnell, Glassmeier, & McFadden, 2008; Pritchett, 2008; Yoo, Yamada, Ji, Jara-Almonte, & Myers, 2014). Excluding this variation, the guide field strength is about 14 nT. Considering the asymmetry (Cassak & Shay, 2007), $B_{\rm rec}$ is about 28 nT. Thus, $B_{\rm g} \sim 0.5 B_{\rm rec}$.

Near the region A, as shown in Fig. 1 (b) and (c), fluctuations in the magnetic field $\mathbf{B}$ below the local lower hybrid frequency ($f_{\rm LH}$, denoted by the black line in (c)) exist. Fluctuations in the electric field $\mathbf{E}$ and electron density $n_{\rm e}$ are not strong, as shown in Fig. 1 (d) and (f). Around the region B, as shown in Fig. 1(b)–(f), there are fluctuations in $\mathbf{B}$, $\mathbf{E}$, and $n_{\rm e}$ near $f_{\rm LH}$. As shown in spectrograms of $\mathbf{B}$ and $\mathbf{E}$ in Fig. 1(c) and (e), most power of the fluctuations exist close to $f_{\rm LH}$.

Figures 1(g) and (h) shows the profile of $\beta_{\rm e}$ and the electron flow vector $\mathbf{u}_{\rm e}$, respectively. Values of $\beta_{\rm e}$ are different in two regions; about 4.2 in A and 0.6 in B. Values of $\mathbf{u}_{\rm e}$, in contrast, are similar. Note that both the perpendicular and parallel components of $\mathbf{u}_{\rm e}$ are significant. The observed features of fluctuations in the region B can be explained by the short-wavelength LHDW. First, the perpendicular electron flow $\mathbf{u}_{e\perp}$ is large. Second, the mode exists when $\beta_{\rm e}$ is small. Finally, the frequency of the wave is around $f_{\rm LH}$.

3 Calculation of the LHDW dispersion relation

The geometry of our local model is similar to that of H. Ji et al. (2005); z is along $\mathbf{B}_0$, and y is along the density gradient direction in the ion rest frame. The wave vector is assumed on the x-z plane with an assumption of negligible k_y. Unlike H. Ji et al. (2005), the equilibrium electron flow velocity ($\mathbf{u}_{\mathrm{e0}}$) has a parallel component ($u_{\mathrm{e0}z}$). Equilibrium temperature is assumed to be uniform and ion temperature anisotropy is ignored.

The detailed derivation of the dispersion relation is provided in the supporting information. Here only important improvements over the model in H. Ji et al. (2005) are discussed. First, for the quasi-electrostatic nature of the short-wavelength LHDW, the perturbed electron density n_{e1} is independently obtained from the electron continuity equation:

$$(\omega - \mathbf{k}\cdot\mathbf{u}_{\mathrm{e0}})n_{\mathrm{e1}} = (\mathbf{k}\cdot\mathbf{u}_{\mathrm{e1}} - i\epsilon u_{\mathrm{e1}y})n_{\mathrm{e0}}, \tag{1}$$

where the subscript 1 indicates perturbed quantities, $\mathbf{u}_{\mathrm{e1}}$ is the perturbed electron flow velocity, n_{e0} is the equilibrium density, and $\epsilon = (dn_{\mathrm{e0}}/dy)/n_{\mathrm{e0}}$ is the inverse of the density gradient scale. The electron temperature anisotropy is also taken into account; $T_{\mathrm{e0}}^{\perp} \neq T_{\mathrm{e0}}^{\parallel}$, where $T_{\mathrm{e0}}^{\perp}$ and $T_{\mathrm{e0}}^{\parallel}$ are the perpendicular and parallel electron equilibrium temperature, respectively.

The perturbed perpendicular electron pressure is assumed to be $p_{\mathrm{e1}}^{\perp} \approx n_{\mathrm{e1}}T_{\mathrm{e0}}^{\perp}$, which means that the perpendicular temperature perturbation is ignored (isothermal limit). This simplification is justifiable because LHDW stability does not much depend on the specific form of $p_{\mathrm{e1}}^{\perp}$; other terms such as $\mathbf{E}_1$, $\mathbf{u}_{\mathrm{e1}}\times\mathbf{B}_0$, and $\mathbf{u}_{\mathrm{e0}}\times\mathbf{B}_1$ are more important for the electron momentum balance along the perpendicular direction. Here, $\mathbf{E}_1$ and $\mathbf{B}_1$ are the perturbed electric and magnetic field, respectively. This isothermal limit implies infinite heat flux for the perpendicular temperature. We find that the dispersion relation does not change much even in the limit of the zero heat flux.

For the parallel direction, however, more rigorous treatment of the electron heat flux is required, as the perturbed electron parallel pressure $p_{\mathrm{e1}}^{\parallel}$ becomes important for the electron force balance due to the absence of $\mathbf{u}_{\mathrm{e1}}\times\mathbf{B}_0$ term. To obtain $p_{\mathrm{e1}}^{\parallel}$, we start from the following equation from the Vlasov equation:

$$\frac{\partial p_{\mathrm{e}}^{\parallel}}{\partial t} + \nabla\cdot(\mathbf{u}_{\mathrm{e}}p_{\mathrm{e}}^{\parallel}) + \nabla\cdot\mathbf{q}_{\mathrm{e}}^{\parallel} + 2\frac{\partial u_{\mathrm{e}z}}{\partial z}p_{\mathrm{e}}^{\parallel} = 0, \tag{2}$$

where $p_{\mathrm{e}}^{\parallel} = m_{\mathrm{e}}\int(v_z - u_{\mathrm{e}z})^2 f_{\mathrm{e}}d\mathbf{v}$, $\mathbf{q}_{\mathrm{e}}^{\parallel} = m_{\mathrm{e}}\int(\mathbf{v}-\mathbf{u}_{\mathrm{e}})(v_z - u_{\mathrm{e}z})^2 f_{\mathrm{e}}d\mathbf{v}$, and $n_{\mathrm{e}}\mathbf{u}_{\mathrm{e}} = \int\mathbf{v}f_{\mathrm{e}}d\mathbf{v}$. Note that $\mathbf{q}_{\mathrm{e}}^{\parallel}$ is the electron heat flux affecting the parallel electron temperature rather than the parallel heat flux.

A closure for $\mathbf{q}_\mathrm{e}^{\|}$ is required for $p_\mathrm{e1}^{\|}$. The 3+1 fluid model (J.-Y. Ji & Joseph, 2018) gives

$$\mathbf{q}_\mathrm{e}^{\|} = \frac{\hat{z}}{m_\mathrm{e}\omega_\mathrm{ce}} \times \left(p_\mathrm{e}^{\|}\nabla T_\mathrm{e} + T_\mathrm{e}\nabla p_\mathrm{e}^{\|} - \frac{T_\mathrm{e}}{2}\nabla \pi_\mathrm{e}^{\|} - T_\mathrm{e}^{\|}\nabla p_\mathrm{e}^{\perp} \right) + q_{\mathrm{e}z}^{\|}\hat{z}, \tag{3}$$

where $\pi_\mathrm{e}^{\|} = 2(p_\mathrm{e}^{\|} - p_\mathrm{e}^{\perp})/3$, and $T_\mathrm{e} = (2T_\mathrm{e}^{\perp} + T_\mathrm{e}^{\|})/3$. The derivation of this equation is also given in the supporting information. The closure for $q_{\mathrm{e}1z}^{\|}$ in the collisionless limit is J.-Y. Ji and Joseph (2018)

$$q_{\mathrm{e}1z}^{\|} = \frac{-i}{\sqrt{\pi}} \frac{k_\|}{|k_\||} 2n_0 v_\mathrm{te} T_\mathrm{e1}^{\|}, \tag{4}$$

where $T_\mathrm{e1}^{\|} = (p_\mathrm{e1}^{\|} - T_\mathrm{e0}^{\|} n_1)/n_0$ is the perturbed parallel temperature and $v_\mathrm{te} = \sqrt{2T_\mathrm{e0}/m_\mathrm{e}}$ is the electron thermal speed. By linearizing Eq. 3, $q_{\mathrm{e}1x}^{\|}$ becomes

$$q_{\mathrm{e}1x}^{\|} = -\frac{2}{9}\frac{(T_\mathrm{e0}^{\|} - 4T_\mathrm{e0}^{\perp})T_\mathrm{e1}^{\|}}{T_\mathrm{e0}^{\perp} + T_\mathrm{i0}} n_0 u_{\mathrm{e}0x} = r_\mathrm{e}^{\|} T_\mathrm{e1}^{\|} n_0 u_{\mathrm{e}0x}, \tag{5}$$

where $r_\mathrm{e}^{\|} = 2(4T_\mathrm{e0}^{\perp} - T_\mathrm{e0}^{\|})/9(T_\mathrm{e0}^{\perp} + T_\mathrm{i0})$. With Eqs. 2, 4, and 5, $p_\mathrm{e1}^{\|}$ is given by

$$p_\mathrm{e1}^{\|} = n_\mathrm{e1} T_\mathrm{e0}^{\|} + \frac{2k_\| n_0 T_\mathrm{e0}^{\|} u_{\mathrm{e}1z}}{\omega - \mathbf{k}\cdot\mathbf{u}_\mathrm{e0} - r_\mathrm{e}^{\|} k_\perp u_{\mathrm{e}0x} + i(2/\sqrt{\pi})|k_\||v_\mathrm{te}}. \tag{6}$$

With these closures, the electron momentum equation is solved to obtain the perturbed electron current density, $\mathbf{J}_\mathrm{e1}$. The ion current is given by the Eq. (8) in the Ref. (H. Ji et al., 2005). With $\mathbf{J}_1 = \mathbf{J}_\mathrm{e1} + \mathbf{J}_\mathrm{i1}$, the Maxwell equation without the displacement current $\mathbf{k} \times (\mathbf{k} \times \mathbf{E}_1) = -i\omega\mu_0\mathbf{J}_1$ can be expressed as

$$\begin{pmatrix} D_{xx} & D_{xy} & D_{xz} \\ D_{yx} & D_{yy} & D_{yz} \\ D_{zx} & D_{zy} & D_{zz} \end{pmatrix} \begin{pmatrix} E_{1x} \\ E_{1y} \\ E_{1z} \end{pmatrix} = 0, \tag{7}$$

with a tensor $\mathbf{D}$. The dispersion relation for the wave can be obtained from $\det \mathbf{D} = 0$. The calculation for each component of $\mathbf{D}$ is provided in the supporting information.

Dispersion relations are obtained with plasma parameters measured in the region A and B. For the region A, parameters averaged over 01:17:39.989–01:17:40.049 are $B_0 =$ 6.5 nT, $n_0 = 6.1$ cm^{-3}, $T_\mathrm{e0}^{\|} = 79.5$ eV, $T_\mathrm{e0}^{\perp} = 70.9$ eV, $T_\mathrm{i0} = 395$ eV, $u_{\mathrm{e}0x} = 17.9V_\mathrm{A}$, and $u_{\mathrm{e}0z} = -14.1V_\mathrm{A}$, where $V_\mathrm{A} = 57.7$ km/s is the local Alfvén speed. With these values, $\beta_\mathrm{e} = 4.24$ and $f_\mathrm{LH} = 4.4$ Hz. For the region B, parameters averaged over 01:17:40.469 – 529 are $B_0 = 19.8$ nT, $n_0 = 6.2$ cm^{-3}, $T_\mathrm{e0}^{\|} = 122$ eV, $T_\mathrm{e0}^{\perp} = 77.6$ eV, $T_\mathrm{i0} = 402$ eV, $u_{\mathrm{e}0x} = 2.65V_\mathrm{A}$, and $u_{\mathrm{e}0z} = -5.07V_\mathrm{A}$ with $V_\mathrm{A} = 174$ km/s, $\beta_\mathrm{e} = 0.58$, and $f_\mathrm{LH} = 12.9$ Hz.

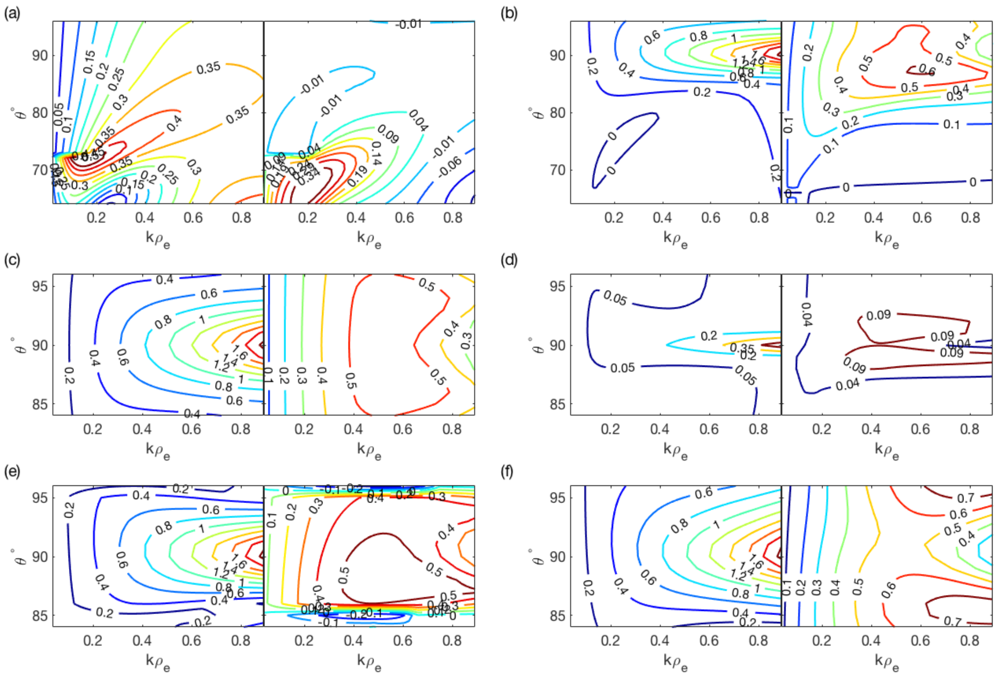

Figure 2. Dispersion relation of LHDW. For each subplot, the left (right) panel shows the contour plot for the real (imaginary) part of the angular frequency normalized by the local lower hybrid frequency ω_{LH} as a function of $k\rho_{\mathrm{e}}$ and θ. Here ρ_{e} is the electron gyroradius in the region B even for the axis of panels (a). (a) In the region A, the long-wavelength LHDW ($\theta \sim 70^\circ$ is unstable, while the short-wavelength LHDW is marginally stable due to high β. (b) In the region B, the short-wavelength LHDW has fast growth rates $\gamma \sim 0.6\omega_{\mathrm{LH}}$ with $\Re(\omega) \sim \omega_{\mathrm{LH}}$. (c) Without the parallel flow, the dispersion becomes symmetric with respect to $\theta = 90^\circ$ but there is no significant change in γ. (d) When the perpendicular flow is reduced to $0.7V_{\mathrm{A}}$, γ becomes much smaller, which indicates $u_{\mathrm{e0}x}$ is the free energy source. The range of θ is different for panels (c) and (d). (e) Without $\mathbf{q}_{\mathrm{e}}^{\parallel}$, oblique modes are stabilized. (f) Without $T_{\mathrm{e1}}^{\parallel}$ (infinite heat flux), γ becomes even larger especially for more oblique modes, which shifts $\Re(\omega)$ with the maximum γ to about $0.4\omega_{\mathrm{LH}}$.

The calculated dispersion relation is shown in Fig. 2(a); the left (right) panel shows the real (imaginary) part of the angular frequency as a function of k and θ, which is normalized by the local (angular) lower hybrid frequency, $\omega_{\rm LH}$. In the region A, the short-wavelength LHDW around $\theta = 90°$ is marginally stable despite the strong electron flow. The long-wavelength LHDW around $\theta = 70°$, in contrast, is unstable around $f < 0.5 f_{\rm LH}$, which agrees with measurements in Fig. 1(c).

In the region B, the short-wavelength LHDW has large growth rates with the maximum growth rate $\gamma_{\rm max} \sim 0.6\omega_{\rm LH}$, as shown in Fig. 2(b). The frequency around $\gamma_{\rm max}$ is $\sim 0.8 f_{\rm LH}$. The model expects $k_\perp \gg |k_\parallel|$. All these features are consistent with those of the short-wavelength LHDW (Davidson et al., 1977).

This model indicates that the free energy source is the perpendicular current. Even with zero parallel electron velocity, the dispersion expects similar γ, as shown in Fig. 2(c). When the perpendicular velocity is decreased from $2.65V_{\rm A}$ to $0.7V_{\rm A}$, however, γ becomes small, as shown in Fig. 2(d). If $u_{{\rm e}0x}$ is reduced below $0.5V_{\rm A}$, the mode disappears.

To understand the effect of $\mathbf{q}_{\rm e}^{\parallel}$ on the dispersion, we have tested two limits – no heat flux and infinite heat flux. Without the heat flux, $p_{\rm e1}^{\parallel}$ in Eqn. 6 becomes

$$p_{\rm e1}^{\parallel} = n_{\rm e1} T_{\rm e0}^{\parallel} + \frac{2k_\parallel n_0 T_{\rm e0}^{\parallel} u_{{\rm e1}z}}{\omega - \mathbf{k}\cdot\mathbf{u}_{\rm e0}}. \tag{8}$$

With the infinite heat flux ($v_{th} \to \infty$), $p_{\rm e1}^{\parallel} = n_{\rm e1} T_{\rm e0}^{\parallel}$, which means $T_{\rm e1}^{\parallel} = 0$. Figure 2 (e) and (f) show the dispersion for these two limits. When θ is close to $90°$, results are not affected. For oblique modes, however, the heat flux significantly affects the dispersion relation, especially the growth rate. Without $\mathbf{q}_{\rm e}^{\parallel}$, oblique modes are quickly stabilized; as shown in the bottom panel of Fig. 2(e), γ becomes negative for $\theta \sim 85°$ or $\theta \sim 96°$. With the infinite heat flux (zero $T_{\rm e1}^{\parallel}$), on the other hand, γ for oblique modes becomes larger than values in Fig. 2(b), as shown in Fig. 2(f).

This dependence of γ on $\mathbf{q}_{\rm e}^{\parallel}$ can be understood by the parallel force balance. The perturbed pressure term, $ikp_{\rm e1}^{\parallel}$ can be interpreted as a restoring force against the electric field perturbation. The heat flux reduces the temperature perturbation, which means that the restoring force decreases as the heat flux increases. Thus, in the limit of the infinite (zero) heat flux, γ becomes larger (smaller) for oblique modes.

4 Comparison between theory and observation

The dispersion relation is crucial for identifying the wave and understanding its propagation. If all MMS satellites observed the same wave packet, $\mathbf{k}$ could be estimated di-

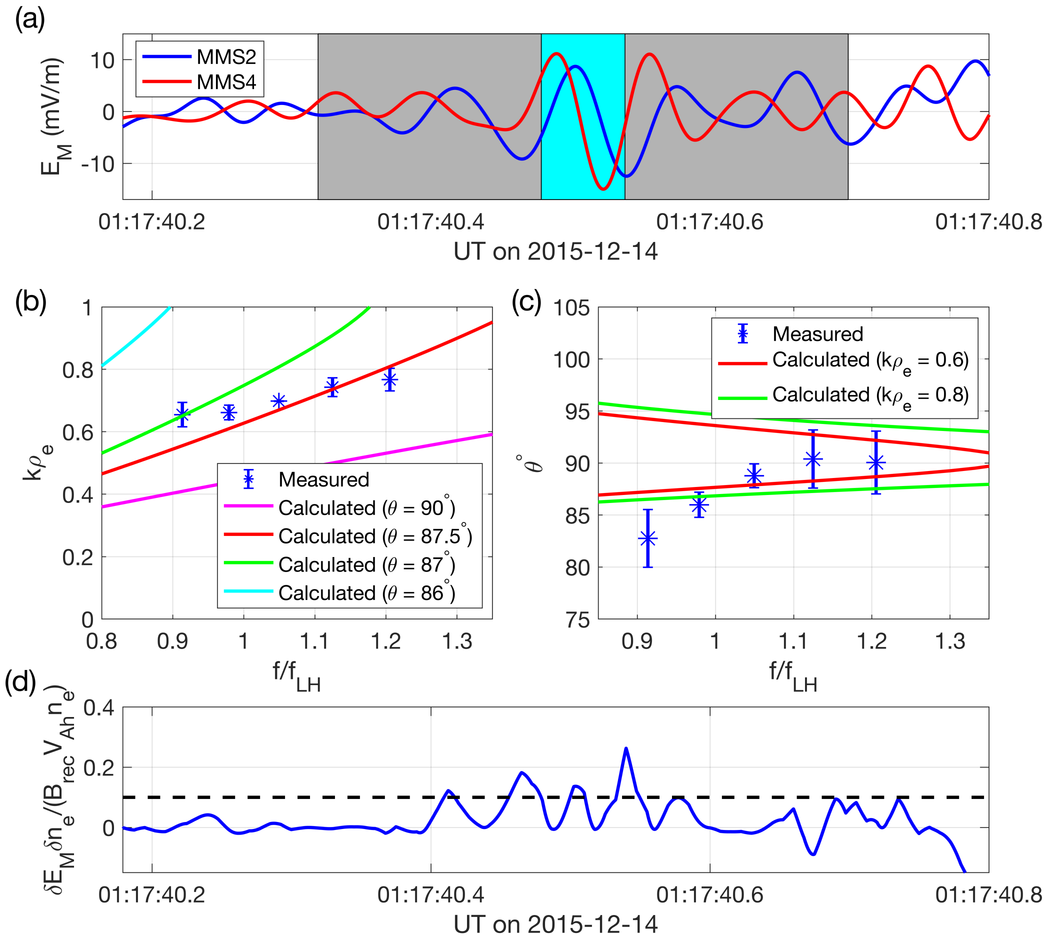

Figure 3. Wave vector measurement and comparison with the theory. (a) Profile of E_M near the region B, which is filtered by a low-pass filter with a cutoff frequency of 40 Hz. Signals from MMS2 and MMS4 correlate. The cyan box indicates the period where the analysis for the wave vector is performed. The gray box indicates the range of data used for the wavelet analysis. (b) Magnitude of the wave vector. Blue asterisks are measured values ($k\rho_\mathrm{e} \sim 0.7$). Theoretical values with various θ are plotted with solid lines. (c) Angle between $\mathbf{k}$ and $\mathbf{B}_0$. Blue asterisks are values estimated by the SVD analysis. Theoretical values with various k are plotted with solid lines. The wave propagates almost perpendicular to $\mathbf{B}_0$. Error bars in (b) and (c) are from the standard deviation of the values computed during the period indicated by the cyan box in (a). Frequency values in (b) and (c) are the central frequency of the Morlet wavelet. (d) Anomalous drag by LHDW. $\delta E_M \delta n_\mathrm{e}$ is normalized by $B_\mathrm{rec} V_\mathrm{Ah} n_\mathrm{e}$. The black dashed line represents the nominal normalized reconnection rate for collisionless reconnection, 0.1 (Birn et al., 2001).

rectly from the phase difference (Yoo et al., 2018). However, for this event, signals from only MMS2 and MMS4 have correlation, while they are near the region B. Thus, single spacecraft methods such as the singular value decomposition (SVD) analysis (Santolík, Parrot, & Lefeuvre, 2003) should be considered.

The SVD analysis has its own caveat; this method relies on the assumption that there is only one dominant $\mathbf{k}$ for a given frequency. This assumption is not valid for LHDW; as shown in Fig. 2(b), there is a range of k and θ that has a positive growth rate for a given frequency. In this case, the estimated $\mathbf{k}$ is a power-weighted average of multiple wave vectors, which underestimates the magnitude of $\mathbf{k}$ (Yoo et al., 2019). The direction of the estimated $\mathbf{k}$, on the other hand, still indicates the average propagation direction.

The wave vector $\mathbf{k}$ is estimated by combining two methods. With the unit vector $\hat{\mathbf{k}}$ from the SVD analysis, the magnitude k is

$$k = \frac{\phi_2 - \phi_4}{\hat{\mathbf{k}} \cdot (\mathbf{r}_2 - \mathbf{r}_4)}, \tag{9}$$

where ϕ_2 and ϕ_4 are the phase of the correlated signal measured by MMS2 and MMS4, while $\mathbf{r}_2$ and $\mathbf{r}_4$ are the location of MMS2 and MMS4, respectively. The phase information comes from the Morlet wavelet transform of E_M (Torrence & Compo, 1998). As shown in Fig. 3(a), E_M signals from two satellites are correlated in the region B (cyan box).

Figure 3(b) shows the measured $k\rho_{\rm e}$ (blue asterisks), compared with theoretical values (solid lines). For theoretical values, the Doppler shift due to the frame difference is considered, which is $\Delta f = \mathbf{u}_{\rm i} \cdot \mathbf{k}/2\pi$. Here $\mathbf{u}_{\rm i}$ is the ion flow velocity in the spacecraft frame ($u_{{\rm i}x} = 33$ km/s, $u_{{\rm i}z} = -38$ km/s). At $f = 0.98 f_{\rm LH}$, $k\rho_{\rm e} = 0.66$, which agrees with the theoretical value with $\theta \sim 87°$. Note that the mode with the highest growth rate exists around $\theta \sim 87°$ and $k\rho_{\rm e} \sim 0.6$, as shown in Fig. 2(b).

Figure 3(c) shows the measured θ (blue asterisks), compared with theoretical values of various k (solid lines). The measurement shows that LHDW propagates almost perpendicular to $\mathbf{B}_0$, which agrees with the model. The measured $\hat{\mathbf{k}}$ has a dominant component along the x direction ($\hat{\mathbf{k}} = (0.987, -0.155, -0.019)$ for $f = 1.05 f_{\rm LH}$), which supports the ignorance of k_y.

The short-wavelength LHDW generates correlated fluctuations of the electron density and electric field, generating anomalous drag force between electrons and ions (Mozer, Wilber, & Drake, 2011). Figure 3(d) shows $\delta E_M \delta n_{\rm e}$, normalized by $B_{\rm rec} V_{\rm Ah} \langle n_{\rm e} \rangle$, where $V_{\rm Ah} = 274$ km/s is the hybrid upstream Alfvén velocity for asymmetric reconnection

(Cassak & Shay, 2007). Here the angle bracket means the average of a quantity A from 01:17:40.2 to 01:17:40.8 and a fluctuating quantity is defined as $\delta A = A - \langle A \rangle$. Two fluctuating quantities δE_M and δn_e are correlated, producing a positive net value of $\delta E_M \delta n_\mathrm{e}$, especially from 01:17:40.4 to 01:17:40.6. The value of $\delta E_M \delta n_\mathrm{e}/\langle n_\mathrm{e} \rangle$ over this period is significant, compared to the nominal reconnection rate for collisionless reconnection, $0.1 B_\mathrm{rec} V_\mathrm{Ah}$ (Birn et al., 2001), indicating a potential importance of the electrostatic LHDW for electron and reconnection dynamics.

5 Summary and Discussions

In summary, we present LHDW activity inside a reconnecting current sheet measured by MMS with a moderate guide field. The long-wavelength LHDW exists inside the EDR where β_e is high, while the short-wavelength LHDW exists slightly outside the EDR where β_e is low. The analysis on the wave number $\mathbf{k}$ shows that $\mathbf{k}$ has a dominant perpendicular component with a magnitude of $k\rho_\mathrm{e} \sim 0.7$ for $f \sim f_\mathrm{LH}$, which agrees with features of the fast-growing, short-wavelength LHDW (Davidson et al., 1977). For better understanding of LHDW, we have developed a local theoretical model for the dispersion relation. Overall, results from this model explains the observed LHDW activity, including the magnitude and direction of $\mathbf{k}$.

The model is based on the previous work in H. Ji et al. (2005) but improved to include the electron heat flux for better modeling of the perturbed parallel electron pressure, electron temperature anisotropy, parallel electron flow, and independent computation of the perturbed electron density for electrostatic effects. This model can calculate the dispersion with an arbitrary angle between the wave vector and magnetic field, unlike the kinetic treatment of LHDW (Davidson et al., 1977).

The limitation of this local model should be discussed. This analysis assumes no wave propagation along the gradient direction, neglecting the global structure of the current sheet. To address this issue, a global eigenmode analysis (Daughton, 2003; **?**) should be carried out, which is our future work. For this event with a large current sheet width, however, this local analysis seems acceptable. The negligible k_y over k_x is also supported by the measurement.

This model assumes no temperature gradient for both electrons and ions but the temperature gradient may be important for LHDW activity. With parameters measured in the region B, however, the results are not sensitive against relatively small change in the local temperature.

This study shows that the short-wavelength LHDW is potentially important for electron and reconnection dynamics by generating drag force between electrons and ions under a sufficient guide field. Further systematic research on this topic within or near the EDR is warranted both in space (i.e. Chen et al., 2019) and in laboratory (i.e. Stechow et al., 2018).

Acknowledgments

This work was supported by DOE Contract No. DE-AC0209CH11466, NASA grants NNH14AX63I and NNH15AB29I, NSF grants AGS-1552142, AGS-1619584, DOE grant DESC0016278, NSF-DOE partnership in plasma science grant DE-FG02-00ER54585, and the NASA MMS mission. All MMS data used are available at https://lasp.colorado.edu/mms/sdc/public/.

References

Birn, J., Drake, J. F., Shay, M. A., Rogers, B. N., Denton, R. E., Hesse, M., … Pritchett, P. L. (2001). Geospace environmental modeling (gem) magnetic reconnection challenge. *J. Geophys. Res.*, *106*, 3715. doi: doi:10.1029/1999JA900449

Carter, T. A., Ji, H., Trintchouk, F., Yamada, M., & Kulsrud, R. M. (2001, Dec). Measurement of lower-hybrid drift turbulence in a reconnecting current sheet. *Phys. Rev. Lett.*, *88*, 015001. Retrieved from `http://link.aps.org/doi/10.1103/PhysRevLett.88.015001` doi: 10.1103/PhysRevLett.88.015001

Cassak, P. A., & Shay, M. A. (2007). Scaling of asymmetric magnetic reconnection: General theory and collisional simulations. *Phys. Plasmas*, *14*(10), 102114. Retrieved from `http://link.aip.org/link/?PHP/14/102114/1` doi: 10.1063/1.2795630

Chen, L.-J., Hesse, M., Wang, S., Gershman, D., Ergun, R. E., Burch, J., … Avanov, L. (2017). Electron diffusion region during magnetopause reconnection with an intermediate guide field: Magnetospheric multiscale observations. *Journal of Geophysical Research: Space Physics*, *122*(5), 5235-5246. Retrieved from `https://agupubs.onlinelibrary.wiley.com/doi/abs/10.1002/2017JA024004` doi: 10.1002/2017JA024004

Chen, L.-J., Wang, S., Hesse, M., Ergun, R. E., Moore, T., Giles, B., ... Lindqvist, P.-A. (2019). Electron diffusion regions in magnetotail reconnection under varying guide fields. *Geophysical Research Letters*, *46*(12), 6230-6238. Retrieved from https://agupubs.onlinelibrary.wiley.com/doi/abs/10.1029/2019GL082393 doi: 10.1029/2019GL082393

Daughton, W. (2003). Electromagnetic properties of the lower-hybrid drift instability in a thin current sheet. *Phys. Plasmas*, *10*(8), 3103–3119. Retrieved from http://scitation.aip.org/content/aip/journal/pop/10/8/10.1063/1.1594724 doi: http://dx.doi.org/10.1063/1.1594724

Davidson, R., Gladd, N., Wu, C., & Huba, J. (1977). Effects of finite plasma beta on the lower-hybrid drift instability. *Phys. Fluids*, *20*, 301.

Ergun, R. E., Chen, L.-J., Wilder, F. D., Ahmadi, N., Eriksson, S., Usanova, M. E., ... Wang, S. (2017). Drift waves, intense parallel electric fields, and turbulence associated with asymmetric magnetic reconnection at the magnetopause. *Geophys. Res. Lett.*, *44*(7), 2978–2986. Retrieved from http://dx.doi.org/10.1002/2016GL072493 doi: 10.1002/2016GL072493

Ergun, R. E., Tucker, S., Westfall, J., Goodrich, K. A., Malaspina, D. M., Summers, D., ... Cully, C. M. (2016, Mar 01). The axial double probe and fields signal processing for the mms mission. *Space Science Reviews*, *199*(1), 167–188. Retrieved from https://doi.org/10.1007/s11214-014-0115-x doi: 10.1007/s11214-014-0115-x

Fox, W., Sciortino, F., v. Stechow, A., Jara-Almonte, J., Yoo, J., Ji, H., & Yamada, M. (2017, Mar). Experimental verification of the role of electron pressure in fast magnetic reconnection with a guide field. *Phys. Rev. Lett.*, *118*, 125002. Retrieved from https://link.aps.org/doi/10.1103/PhysRevLett.118.125002 doi: 10.1103/PhysRevLett.118.125002

Graham, D. B., Khotyaintsev, Y. V., Norgren, C., Vaivads, A., André, M., Toledo-Redondo, S., ... Burch, J. L. (2017). Lower hybrid waves in the ion diffusion and magnetospheric inflow regions. *J. Geophys. Res.*, *122*(1), 517–533. Retrieved from http://dx.doi.org/10.1002/2016JA023572 (2016JA023572) doi: 10.1002/2016JA023572

Haaland, S. E., Sonnerup, B. U. Ö., Dunlop, M. W., Balogh, A., Georgescu, E., Hasegawa, H., ... Vaivads, A. (2004). Four-spacecraft determination of magnetopause orientation, motion and thickness: comparison with results from single-spacecraft methods. *Ann. Geophys.*, *22*(4), 1347–1365. Retrieved from http://www.ann-geophys.net/22/1347/2004/ doi: 10.5194/angeo-22-1347-2004

Ji, H., Kulsrud, R., Fox, W., & Yamada, M. (2005). An obliquely propagating electromagnetic drift instability in the lower hybrid frequency range. *J. Geophys. Res.*, *110*, A08212.

Ji, H., Terry, S., Yamada, M., Kulsrud, R., Kuritsyn, A., & Ren, Y. (2004, Mar). Electromagnetic fluctuations during fast reconnection in a laboratory plasma. *Phys. Rev. Lett.*, *92*, 115001. Retrieved from http://link.aps.org/doi/10.1103/PhysRevLett.92.115001 doi: 10.1103/PhysRevLett.92.115001

Ji, J.-Y., & Joseph, I. (2018). Electron parallel closures for the 3 + 1 fluid model. *Phys. Plasmas*, *25*(3), 032117. Retrieved from https://doi.org/10.1063/1.5014996 doi: 10.1063/1.5014996

Le Contel, O., Leroy, P., Roux, A., Coillot, C., Alison, D., Bouabdellah, A., … de la Porte, B. (2016, Mar 01). The search-coil magnetometer for mms. *Space Science Reviews*, *199*(1), 257–282. Retrieved from https://doi.org/10.1007/s11214-014-0096-9 doi: 10.1007/s11214-014-0096-9

Lindqvist, P.-A., Olsson, G., Torbert, R. B., King, B., Granoff, M., Rau, D., … Tucker, S. (2016, Mar 01). The spin-plane double probe electric field instrument for mms. *Space Science Reviews*, *199*(1), 137–165. Retrieved from https://doi.org/10.1007/s11214-014-0116-9 doi: 10.1007/s11214-014-0116-9

Mozer, F. S., Angelopoulos, V., Bonnell, J., Glassmeier, K. H., & McFadden, J. P. (2008). Themis observations of modified hall fields in asymmetric magnetic field reconnection. *Geophys. Res. Lett.*, *35*(17), L17S04. Retrieved from http://dx.doi.org/10.1029/2007GL033033 doi: 10.1029/2007GL033033

Mozer, F. S., Wilber, M., & Drake, J. F. (2011). Wave associated anomalous drag during magnetic field reconnection. *Phys. Plasmas*, *18*(10), 102902. Retrieved from http://link.aip.org/link/?PHP/18/102902/1 doi: 10.1063/1.3647508

Norgren, C., Vaivads, A., Khotyaintsev, Y. V., & André, M. (2012, Jul). Lower hybrid drift waves: Space observations. *Phys. Rev. Lett.*, *109*, 055001. Retrieved from https://link.aps.org/doi/10.1103/PhysRevLett.109.055001 doi: 10.1103/PhysRevLett.109.055001

Pollock, C., Moore, T., Jacques, A., Burch, J., Gliese, U., Saito, Y., ... Zeuch, M. (2016, Mar 01). Fast plasma investigation for magnetospheric multiscale. *Space Science Reviews*, *199*(1), 331–406. Retrieved from https://doi.org/10.1007/s11214-016-0245-4 doi: 10.1007/s11214-016-0245-4

Pritchett, P. L. (2008). Collisionless magnetic reconnection in an asymmetric current sheet. *J. Geophys. Res.*, *113*(A6), A06210. Retrieved from http://dx.doi.org/10.1029/2007JA012930 doi: 10.1029/2007JA012930

Pritchett, P. L., & Coroniti, F. V. (2004, January). Three-dimensional collisionless magnetic reconnection in the presence of a guide field. *J. Geophys. Res.*, *109*, 1220.

Ricci, P., Blackbill, J., Daughton, W., & Lapenta, G. (2004). Influence of the lower hybrid drift instability on the onset of magnetic reconnection. *Phys. Plasmas*, *11*, 4489.

Roytershteyn, V., Daughton, W., Karimabadi, H., & Mozer, F. S. (2012, May). Influence of the lower-hybrid drift instability on magnetic reconnection in asymmetric configurations. *Phys. Rev. Lett.*, *108*, 185001. Retrieved from http://link.aps.org/doi/10.1103/PhysRevLett.108.185001 doi: 10.1103/PhysRevLett.108.185001

Roytershteyn, V., Dorfman, S., Daughton, W., Ji, H., Yamada, M., & Karimabadi, H. (2013). Electromagnetic instability of thin reconnection layers: Comparison of three-dimensional simulations with mrx observations. *Phys. Plasmas*, *20*(6), -. Retrieved from http://scitation.aip.org/content/aip/journal/pop/20/6/10.1063/1.4811371 doi: http://dx.doi.org/10.1063/1.4811371

Russell, C. T., Anderson, B. J., Baumjohann, W., Bromund, K. R., Dearborn, D., Fischer, D., ... Richter, I. (2016, Mar 01). The magnetospheric multiscale magnetometers. *Space Science Reviews*, *199*(1), 189–256. Retrieved from https://doi.org/10.1007/s11214-014-0057-3 doi: 10.1007/s11214-014-0057-3

Santolík, O., Parrot, M., & Lefeuvre, F. (2003). Singular value decomposition methods for wave propagation analysis. *Radio Science*, *38*(1), 1010. Retrieved from http://dx.doi.org/10.1029/2000RS002523 doi: 10.1029/2000RS002523

Stechow, A. v., Fox, W., Jara-Almonte, J., Yoo, J., Ji, H., & Yamada, M. (2018). Electromagnetic fluctuations during guide field reconnection in a laboratory plasma. *Physics of Plasmas*, *25*(5), 052120. Retrieved from `https://doi.org/10.1063/1.5025827` doi: 10.1063/1.5025827

Tharp, T. D., Yamada, M., Ji, H., Lawrence, E., Dorfman, S., Myers, C. E., & Yoo, J. (2012, Oct). Quantitative study of guide-field effects on hall reconnection in a laboratory plasma. *Phys. Rev. Lett.*, *109*, 165002. Retrieved from `http://link.aps.org/doi/10.1103/PhysRevLett.109.165002` doi: 10.1103/PhysRevLett.109.165002

Torrence, C., & Compo, G. P. (1998). A practical guide to wavelet analysis. *Bulletin of the American Meteorological Society*, *79*(1), 61–78. Retrieved from `https://doi.org/10.1175/1520-0477(1998)079<0061:APGTWA>2.0.CO;2` doi: 10.1175/1520-0477(1998)079⟨0061:APGTWA⟩2.0.CO;2

Yamada, M., Kulsrud, R., & Ji, H. (2010, Mar). Magnetic reconnection. *Rev. Mod. Phys.*, *82*, 603–664. Retrieved from `http://link.aps.org/doi/10.1103/RevModPhys.82.603` doi: 10.1103/RevModPhys.82.603

Yoo, J., Jara-Almonte, J., Yerger, E., Wang, S., Qian, T., Le, A., … Gershman, D. J. (2018). Whistler wave generation by anisotropic tail electrons during asymmetric magnetic reconnection in space and laboratory. *Geophysical Research Letters*, *45*(16), 8054-8061. Retrieved from `https://agupubs.onlinelibrary.wiley.com/doi/abs/10.1029/2018GL079278` doi: 10.1029/2018GL079278

Yoo, J., Wang, S., Yerger, E., Jara-Almonte, J., Ji, H., Yamada, M., … Alt, A. (2019). Whistler wave generation by electron temperature anisotropy during magnetic reconnection at the magnetopause. *Physics of Plasmas*, *26*(5), 052902. Retrieved from `https://doi.org/10.1063/1.5094636` doi: 10.1063/1.5094636

Yoo, J., & Yamada, M. (2012). Experimental evaluation of common spacecraft data analysis techniques for reconnection region analysis in a laboratory plasma. *J. of Geophys. Res.*, *117*(A12), A12202. Retrieved from `http://dx.doi.org/10.1029/2012JA017742` doi: 10.1029/2012JA017742

Yoo, J., Yamada, M., Ji, H., Jara-Almonte, J., & Myers, C. E. (2014). Bulk ion acceleration and particle heating during magnetic reconnection in a laboratory plasma. *Phys. Plasmas*, *21*(5), 055706. Retrieved from `http://scitation.aip.org/content/aip/journal/pop/21/5/10.1063/1.4874331` doi: http://dx.doi.org/10.1063/1.4874331

Yoo, J., Yamada, M., Ji, H., Jara-Almonte, J., Myers, C. E., & Chen, L.-J. (2014, Aug). Laboratory study of magnetic reconnection with a density asymmetry across the current sheet. *Phys. Rev. Lett.*, *113*, 095002. Retrieved from `http://link.aps.org/doi/10.1103/PhysRevLett.113.095002` doi: 10.1103/PhysRevLett.113.095002

Supporting Information of "lower hybrid drift waves during guide field reconnection"

Jongsoo Yoo[1], Jeong-Young Ji[2], M. V. Ambat[3], Shan Wang[4], Hantao Ji[5], Jensen Lo[5], Bowen Li[6], Yang Ren[1], J. Jara-Almonte[1], Li-Jen Chen[4], William Fox[1], Masaaki Yamada[1], Andrew Alt[1], Aaron Goodman[1]

[1]Princeton Plasma Physics Laboratory, Princeton, New Jersey 08543, USA.
[2]Department of Physics, Utah State University, Logan, Utah 84322, USA.
[3]Department of Mechanical Engineering, University of Rochester, Rochester, NY 14627, USA.
[4]NASA Goddard Space Flight Center, Greenbelt, Maryland 20771, USA.
[5]Department of Astrophysical Sciences, Princeton University, Princeton, NJ 08544, USA.
[6]Harbin Institute of Technology, Harbin, China.

1 Derivation of $\mathbf{q}^{\parallel}$ (Eqn. 12)

From the kinetic equation in the $(t, \mathbf{r}, \mathbf{w} \equiv \mathbf{v} - \mathbf{V}))$ coordinates ($\mathbf{V}$ is the fluid velocity),

$$\frac{df}{dt} - (\mathbf{w} \cdot \nabla \mathbf{V}) \cdot \frac{\partial}{\partial \mathbf{w}} f + \nabla \cdot (\mathbf{w} f) + \frac{\partial}{\partial \mathbf{w}} \cdot (\mathbf{A} f) + \frac{q}{m} \mathbf{w} \times \mathbf{B} \cdot \frac{\partial}{\partial \mathbf{w}} f = C(f), \tag{1}$$

where

$$\frac{d}{dt} = \frac{\partial}{\partial t} + \mathbf{V} \cdot \nabla, \tag{2}$$

$$\mathbf{A} = \frac{1}{m}[\mathbf{F}_* + q(\mathbf{V} \times \mathbf{B})] - \frac{d\mathbf{V}}{dt}. \tag{3}$$

For the $p^{\parallel}$ fluid equation, we need to obtain the closure

$$\mathbf{q}^{\parallel} = \int d^3 v m w_{\parallel}^2 \mathbf{w} f = q_{\parallel}^{\parallel} \hat{z} + \mathbf{q}_{\perp}^{\parallel} \tag{4}$$

where $q_{\parallel}^{\parallel} = \int d^3 v m w_{\parallel}^3 f$ has been obtained in J.-Y. Ji and Joseph (2018) and we will obtain the $\mathbf{q}_{\perp}^{\parallel}$ closure. We adopt the closure (transport) ordering $d/dt \approx 0$ and the linear response theory.

We take the moments $\int d^3 v m w_{\parallel}^2 \mathbf{w}$ of the kinetic equation:

$$\int d^3 v m w_{\parallel}^2 \mathbf{w} \frac{df}{dt} = \frac{d}{dt} \mathbf{q}^{\parallel} \text{ : ignored by the closure ordering,} \tag{5}$$

$$\int d^3 v m w_{\parallel}^2 \mathbf{w} (\mathbf{w} \cdot \nabla \mathbf{V}) \cdot \frac{\partial}{\partial \mathbf{w}} f \text{ : ignored by the linearization,} \tag{6}$$

$$\int d^3 v m w_{\parallel}^2 \mathbf{w} \nabla \cdot (\mathbf{w} f) = \nabla \cdot (\hat{z}\hat{z} : \int d^3 v m \mathbf{wwww} f). \tag{7}$$

We should decompose $\mathbf{wwww}$ into orthogonal polynomials (see J.-Y. Ji and Held (2008)) for the consistent truncation in the expansion of a distribution function.

$$\mathbf{c} = \frac{\mathbf{w}}{v_T} = \frac{\mathbf{w}}{\sqrt{2T/m}} \tag{8}$$

$$\begin{aligned} \mathbf{cccc} &= \mathsf{p}^4 + \frac{6}{7}\left(c^2 - \frac{7}{2}\right)\left\{\mathsf{p}^2 \mathsf{I}\right\} + 3\left\{\mathsf{p}^2 \mathsf{I}\right\} + \left(\frac{2}{5}\mathsf{p}^{02} - \mathsf{p}^{01} + \frac{3}{4}\right)\{\mathsf{II}\} \\ &= \mathsf{p}^{40} - \frac{6}{7}\left\{\mathsf{p}^{21}\mathsf{I}\right\} + 3\left\{\mathsf{p}^{20}\mathsf{I}\right\} + \left(\frac{2}{5}\mathsf{p}^{02} - \mathsf{p}^{01} + \frac{3}{4}\right)\{\mathsf{II}\} \\ &= 3\left\{\mathsf{p}^2 \mathsf{I}\right\} + \frac{3}{4}\{\mathsf{II}\} + \text{higher order moments to be truncated,} \end{aligned} \tag{9}$$

where the operator $\{...\}$ is the symmetrization of the tensor (J.-Y. Ji & Held, 2008). For $\mathbf{bb}:\mathbf{cccc}$ (notation $\mathbf{b}=\hat{z}$),

$$\mathbf{bb}:\left\{\mathsf{p}^2\mathsf{I}\right\}=\frac{1}{6}\left(\mathbf{bb}:\mathsf{p}^2\mathsf{I}+2\mathbf{bb}\cdot\mathsf{p}^2+2\mathbf{b}\cdot\mathsf{p}^2\mathbf{b}+\mathsf{p}^2\right), \tag{10}$$

$$\mathbf{bb}:\{\mathsf{II}\}=\frac{1}{3}(\mathsf{I}+2\mathbf{bb}). \tag{11}$$

Therefore,

$$\begin{aligned}\int d\mathbf{v}mw_\parallel^2\mathbf{ww}f &= mv_T^4\int d\mathbf{v}\mathbf{bb}:\left(3\left\{\mathsf{p}^2\mathsf{I}\right\}+\frac{3}{4}\{\mathsf{II}\}\right)f \\ &= mv_T^4\int d\mathbf{v}\left[3\frac{1}{6}\left(\mathbf{bb}:\mathsf{p}^2\mathsf{I}+2\mathbf{bb}\cdot\mathsf{p}^2+2\mathbf{bb}\cdot\mathsf{p}^2+\mathsf{p}^2\right)+\frac{3}{4}\frac{1}{3}(\mathsf{I}+2\mathbf{bb})\right]f \\ &= \frac{v_T^2}{2}\left(\pi_\parallel\mathsf{I}+2\mathbf{bb}\cdot\boldsymbol{\pi}+2\mathbf{b}\cdot\boldsymbol{\pi}\mathbf{b}+\boldsymbol{\pi}\right)+mv_T^4\frac{1}{4}n\left(\mathsf{I}+2\mathbf{bb}\right) \\ &= \frac{T}{m}\left(\pi_\parallel\mathsf{I}+2\mathbf{bb}\cdot\boldsymbol{\pi}+2\mathbf{b}\cdot\boldsymbol{\pi}\mathbf{b}+\boldsymbol{\pi}\right)+T\frac{p}{m}\left(\mathsf{I}+2\mathbf{bb}\right) \\ &= \frac{T}{m}p^\parallel\mathsf{I}+2\frac{T}{m}\mathbf{bb}\cdot\boldsymbol{\pi}+2\frac{T}{m}\mathbf{b}\cdot\boldsymbol{\pi}\mathbf{b}+\frac{T}{m}\boldsymbol{\pi}+T\frac{p}{m}2\mathbf{bb},\end{aligned} \tag{12}$$

where

$$\begin{aligned}p^\parallel &= p+\pi_\parallel, &(13)\\ p^\perp &= p-\frac{1}{2}\pi_\parallel, &(14)\end{aligned}$$

$$\pi_\parallel=\frac{2}{3}(p^\parallel-p^\perp), \tag{15}$$

$$p=\frac{1}{3}\left(p^\parallel+2p^\perp\right), \tag{16}$$

$$\boldsymbol{\pi}=\frac{3}{2}\pi_\parallel(\mathbf{bb}-\frac{1}{3}\mathsf{I}), \tag{17}$$

$$\mathbf{b}\cdot\boldsymbol{\pi}=\pi_\parallel\mathbf{b}. \tag{18}$$

Hereafter we will drop $\mathbf{b}$ terms, which will be nullified by the $\mathbf{b}\times$ operation:

$$\nabla\cdot\boldsymbol{\pi}=\frac{3}{2}\mathbf{b}\partial_\parallel\pi_\parallel-\frac{1}{2}\nabla\pi_\parallel\to-\frac{1}{2}\nabla\pi_\parallel, \tag{19}$$

$$\begin{aligned}\nabla\cdot\int d\mathbf{v}mw_\parallel^2\mathbf{ww}f &\approx \nabla\cdot\left(\frac{T}{m}p^\parallel\mathsf{I}+2\frac{T}{m}\mathbf{bb}\cdot\boldsymbol{\pi}+2\frac{T}{m}\mathbf{b}\cdot\boldsymbol{\pi}\mathbf{b}+\frac{T}{m}\boldsymbol{\pi}+T\frac{p}{m}2\mathbf{bb}\right) \\ &= \nabla\cdot\left(\frac{T}{m}p^\parallel\mathsf{I}+4\frac{T}{m}\pi_\parallel\mathbf{bb}+\frac{T}{m}\boldsymbol{\pi}+T\frac{p}{m}2\mathbf{bb}\right) \\ &\to \frac{1}{m}p^\parallel\nabla T+\frac{1}{m}T\nabla p^\parallel-\frac{T}{2m}\nabla\pi_\parallel.\end{aligned} \tag{20}$$

For the $\frac{\partial}{\partial\mathbf{w}}\cdot(\mathbf{A}f)$ term,

$$\mathbf{A}=\frac{1}{m}[\mathbf{F}_*+q(\mathbf{V}\times\mathbf{B})]-\frac{d\mathbf{V}}{dt}=\frac{1}{mn}(\nabla p+\nabla\cdot\boldsymbol{\pi}). \tag{21}$$

$$\begin{aligned}
\int d\mathbf{v} m w_\|^2 \mathbf{w} \frac{\partial}{\partial \mathbf{w}} \cdot (\mathbf{A} f) &= -\int d\mathbf{v} m \mathbf{A} \cdot \frac{\partial}{\partial \mathbf{w}} (w_\|^2 \mathbf{w}) f \\
&= -\int d\mathbf{v} m (2\mathbf{b} \cdot \mathbf{ww} \mathbf{A} \cdot \mathbf{b} + w_\|^2 \mathbf{A}) f \\
&= -2\mathbf{b} \cdot \mathsf{p} \mathbf{A} \cdot \mathbf{b} - p^\| \mathbf{A} \\
&= -2p^\| \mathbf{A} \cdot \mathbf{bb} - p^\| \mathbf{A} \\
&\to -p^\| \frac{1}{mn} (\nabla p + \nabla \cdot \boldsymbol{\pi}) \\
&= -p^\| \frac{1}{mn} (\nabla p - \frac{1}{2} \nabla \pi_\| + \frac{3}{2} \mathbf{b} \partial_\| \pi_\|) \\
&\to -\frac{p^\|}{mn} \nabla p^\perp.
\end{aligned} \tag{22}$$

All together, $\nabla \cdot (\mathbf{w} f) + \frac{\partial}{\partial \mathbf{w}} \cdot (\mathbf{A} f)$

$$\begin{aligned}
\mathbf{all} &= \frac{1}{m} p^\| \nabla T + \frac{1}{m} T \nabla p^\| - \frac{T}{2m} \nabla \pi_\| - \frac{p^\|}{mn} \nabla p^\perp \\
&= \frac{1}{m} \left(p^\| \nabla T + T \nabla p^\| - \frac{T}{2} \nabla \pi_\| - \frac{p^\|}{n} \nabla p^\perp \right).
\end{aligned} \tag{23}$$

$$\begin{aligned}
\int d^3 v m w_\|^2 \mathbf{w} \frac{\partial}{\partial \mathbf{w}} \cdot (\mathbf{w} \times \mathbf{B} f) &= -m \int d^3 v \, (\mathbf{w} \times \mathbf{B} f) \cdot \frac{\partial}{\partial \mathbf{w}} \left(w_\|^2 \mathbf{w} \right) \\
&= -m \int d^3 v \, (\mathbf{w} \times \mathbf{B} f) \cdot \left(2 w_\| \mathbf{b} + w_\|^2 \mathsf{I} \right) \\
&= -m \int d^3 v w_\|^2 \mathbf{w} \times \mathbf{B} f \\
&= -\mathbf{q}^\| \times \mathbf{B}.
\end{aligned} \tag{24}$$

$$\frac{q}{m} \int d^3 v m w_\|^2 \mathbf{w} \frac{\partial}{\partial \mathbf{w}} \cdot (\mathbf{w} \times \mathbf{B} f) = -\Omega \mathbf{q}^\| \times \mathbf{b}. \tag{25}$$

The final equation becomes

$$\text{(terms dropped by closure ordering)} + \mathbf{all} + (\text{terms} \quad \propto \quad \mathbf{b}) - \Omega \mathbf{q}^\| \times \hat{z} = 0 \text{ (collisionless)}$$

$$\mathbf{q}_\perp^\| = \frac{1}{\Omega} \hat{z} \times \mathbf{all}. \tag{26}$$

$$\mathbf{q}^\| = \int d\mathbf{v} m w_\|^2 \mathbf{w} f = q_\|^\| \hat{z} + \mathbf{q}_\perp^\|. \tag{27}$$

$$\mathbf{q}_\perp^\| = \frac{1}{m\Omega} \mathbf{b} \times \left(p^\| \nabla T + T \nabla p^\| - \frac{T}{2} \nabla \pi_\| - \frac{p^\|}{n} \nabla p^\perp \right). \tag{28}$$

2 Derivation of the dispersion relation

The geometry of the model is shown in 1. From the equilibrium momentum equations, the equilibrium electric field is

$$E_0 = \frac{T_{\mathrm{i}0}}{T_{\mathrm{e}0}^\perp + T_{\mathrm{i}0}} u_{\mathrm{e}0x} B_0. \tag{29}$$

The inverse of the gradient scale is given by

$$\epsilon = \frac{e u_{\mathrm{e}0x} B_0}{T_{\mathrm{e}0}^\perp + T_{\mathrm{i}0}}. \tag{30}$$

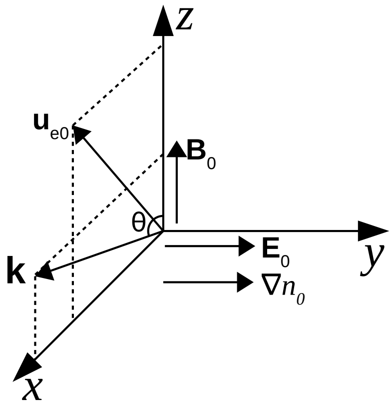

Figure 1. Geometry of the local theory for the LHDW dispersion calculation. The model is in the ion rest frame with z toward the equilibrium magnetic field ($\mathbf{B}_0$) and y along the density gradient direction. The equilibrium electric field $\mathbf{E}_0$ is also along y for the force balance. The equilibrium electron flow velocity $\mathbf{u}_{\mathrm{e0}}$ and wave vector $\mathbf{k}$ reside on the x-z plane. The angle between $\mathbf{k}$ and $\mathbf{B}_0$ is given by θ.

For the dispersion relation, the following Maxwell's equation without the displacement current term is used:

$$\mathbf{k} \times (\mathbf{k} \times \mathbf{E}_1) = -i\omega\mu_0 \mathbf{J}_1. \tag{31}$$

The perturbed ion current density ($\mathbf{J}_{\mathrm{i1}}$) is given by (H. Ji, Kulsrud, Fox, & Yamada, 2005)

$$\mathbf{J}_{\mathrm{i1}} = -\frac{in_0 e^2}{m_{\mathrm{i}} k v_{\mathrm{ti}}} \left[Z(\zeta)\mathbf{E}_1 + \frac{Z''(\mathbf{E}_1 \cdot \hat{\mathbf{k}})}{2}\hat{\mathbf{k}} - i\left(\frac{\epsilon}{2k}\right) Z'' E_{1y}\hat{\mathbf{k}} \right]. \tag{32}$$

The first order electron momentum equation is given by

$$im_{\mathrm{e}} n_0 \left(\omega - \mathbf{k}\cdot\mathbf{u}_{\mathrm{e0}}\right)\mathbf{u}_{\mathrm{e1}} = i\mathbf{k}\cdot\mathbf{P}_{\mathrm{e1}} + en_0(\mathbf{E}_1 + \mathbf{u}_{\mathrm{e1}}\times\mathbf{B}_0 + \mathbf{u}_{\mathrm{e0}}\times\mathbf{B}_1) + e(\mathbf{E}_0 + \mathbf{u}_{\mathrm{e0}}\times\mathbf{B}_0)n_{\mathrm{e1}}. \tag{33}$$

The perturbed electron density n_{e1} is given by the electron continuity equation, which is

$$(\omega - \mathbf{k}\cdot\mathbf{u}_{\mathrm{e0}})n_{\mathrm{e1}} = (\mathbf{k}\cdot\mathbf{u}_{\mathrm{e1}} - i\epsilon u_{\mathrm{e1}y})n_{\mathrm{e0}}. \tag{34}$$

Assuming that the perpendicular temperature perturbation is negligible, $p_{\mathrm{e1}}^{\perp}$ is just

$$p_{\mathrm{e1}}^{\perp} \approx n_{\mathrm{e1}} T_{\mathrm{e0}}^{\perp}. \tag{35}$$

For the parallel electron pressure, the following equation from the Vlasov equation is used:

$$\frac{\partial p_{\mathrm{e}}^{\parallel}}{\partial t} + \nabla\cdot(\mathbf{u}_{\mathrm{e}} p_{\mathrm{e}}^{\parallel}) + \nabla\cdot\mathbf{q}_{\mathrm{e}}^{\parallel} + 2\frac{\partial u_{\mathrm{e}z}}{\partial z} p_{\mathrm{e}}^{\parallel} = 0, \tag{36}$$

where

$$p_{\rm e}^{\parallel} = m_{\rm e}\int (v_z - u_{{\rm e}z})^2 f_{\rm e} d\mathbf{v}, \tag{37}$$

$$\mathbf{q}_{\rm e}^{\parallel} = m_{\rm e}\int (\mathbf{v}-\mathbf{u}_{\rm e})(v_z - u_{{\rm e}z})^2 f_{\rm e} d\mathbf{v}, \tag{38}$$

$$n_{\rm e}\mathbf{u}_{\rm e} = \int \mathbf{v} f_{\rm e} d\mathbf{v}. \tag{39}$$

Linearizing Eqn. 36 yields

$$-i\omega p_{\rm e1}^{\parallel} + \epsilon u_{{\rm e1}y} p_{\rm e0}^{\parallel} + i(\mathbf{k}\cdot\mathbf{u}_{\rm e0})p_{\rm e1}^{\parallel} + i(\mathbf{k}\cdot\mathbf{u}_{\rm e1})n_0 T_{\rm e0}^{\parallel} + i\mathbf{k}\cdot\mathbf{q}_{\rm e1}^{\parallel} + 2ik_{\parallel}u_{{\rm e1}z}n_0 T_{\rm e0}^{\parallel} = 0. \tag{40}$$

As shown in the previous section, the $3+1$ fluid model gives us

$$\mathbf{q}_{\rm e}^{\parallel} = \frac{\hat{z}}{m_{\rm e}\omega_{\rm ce}} \times \left(p_{\rm e}^{\parallel}\nabla T_{\rm e} + T_{\rm e}\nabla p_{\rm e}^{\parallel} - \frac{T_{\rm e}}{2}\nabla \pi_{\rm e}^{\parallel} - T_{\rm e}^{\parallel}\nabla p_{\rm e}^{\perp}\right) + q_{{\rm e}z}^{\parallel}\hat{z}, \tag{41}$$

where $\pi_{\rm e}^{\parallel} = 2(p_{\rm e}^{\parallel} - p_{\rm e}^{\perp})/3$, $T_{\rm e} = (2T_{\rm e}^{\perp} + T_{\rm e}^{\parallel})/3$. The closure for $q_{{\rm e1}z}^{\parallel}$ in the collisionless limit is given by J.-Y. Ji and Joseph (2018)

$$q_{{\rm e1}z}^{\parallel} = \frac{-i}{\sqrt{\pi}}\frac{k_{\parallel}}{|k_{\parallel}|}2n_0 v_{\rm te} T_{\rm e1}^{\parallel}, \tag{42}$$

where $T_{\rm e1}^{\parallel} = (p_{\rm e1}^{\parallel} - T_{\rm e0}^{\parallel} n_1)/n_0$ is the perturbed parallel temperature. Since $k_y = 0$, only $q_{{\rm e1}x}^{\parallel}$ is required to close Eqn. 40. By linearizing Eqn. 41 and using Eqn. 30, $q_{{\rm e1}x}^{\parallel}$ becomes

$$q_{{\rm e1}x}^{\parallel} = -\frac{2}{9}\frac{(T_{\rm e0}^{\parallel} - 4T_{\rm e0}^{\perp})T_{\rm e1}^{\parallel}}{T_{\rm e0}^{\perp} + T_{\rm i0}} n_0 u_{{\rm e0}x} = r_{\rm e}^{\parallel} T_{\rm e1}^{\parallel} n_0 u_{{\rm e0}x}, \tag{43}$$

where $r_{\rm e}^{\parallel} = 2(4T_{\rm e0}^{\perp} - T_{\rm e0}^{\parallel})/9(T_{\rm e0}^{\perp} + T_{\rm i0})$.

Then, $i\mathbf{k}\cdot\mathbf{q}_{\rm e1}^{\parallel}$ becomes

$$i\mathbf{k}\cdot\mathbf{q}_{\rm e1}^{\parallel} = i\left[k_{\perp} r_{\rm e}^{\parallel} u_{{\rm e0}x} - i(2/\sqrt{\pi})|k_{\parallel}|v_{\rm te}\right] n_0(p_{\rm e1}^{\parallel} - T_{\rm e0}^{\parallel} n_1) - ik_{\perp} r_{\rm e}^{\perp} u_{{\rm e0}x} n_0 T_{\rm e1}^{\perp}. \tag{44}$$

Then, from Eqn. 40, $p_{\rm e1}^{\parallel}$ becomes

$$p_{\rm e1}^{\parallel} = n_{\rm e1} T_{\rm e0}^{\parallel} + \frac{2k_{\parallel} n_0 T_{\rm e0}^{\parallel} u_{{\rm e1}z}}{\omega - \mathbf{k}\cdot\mathbf{u}_{\rm e0} - r_{\rm e}^{\parallel} k_{\perp} u_{{\rm e0}x} + i(2/\sqrt{\pi})|k_{\parallel}|v_{\rm te}}. \tag{45}$$

The z component of Eqn. 33 is

$$im_{\rm e} n_0(\omega - \mathbf{k}\cdot\mathbf{u}_{\rm e0})u_{{\rm e1}z} = ik_{\parallel} p_{\rm e1}^{\parallel} + en_0(E_{1z} + u_{{\rm e0}x} B_{1y}), \tag{46}$$

From the Faraday's Law ($\omega\mathbf{B}_1 = \mathbf{k}\times\mathbf{E}_1$), $B_{1y} = (k_{\parallel} E_{1x} - k_{\perp} E_{1z})/\omega$. With Eqn. 45, Eqn. 46, and $\alpha_{\rm e} = (\omega - \mathbf{k}\cdot\mathbf{u}_{\rm e0})/\omega_{\rm ce}$, $u_{{\rm e1}z}$ is expressed as

$$i\alpha_{{\rm e}z} u_{{\rm e1}z} = A_{{\rm e}z} + i\frac{\cos\theta}{2\alpha_{\rm e}}\left(\frac{kv_{\rm te}^{\parallel}}{\omega_{\rm ce}}\right)^2 \left[u_{{\rm e1}x}\sin\theta - i\left(\frac{\epsilon}{k}\right)u_{{\rm e1}y}\right], \tag{47}$$

where

$$\alpha_{{\rm e}z} = \alpha_{\rm e} - \left(\frac{kv_{\rm te}^{\parallel}\cos\theta}{\omega_{\rm ce}}\right)^2 \left[\frac{1}{2\alpha_{\rm e}} + \frac{1}{\alpha_{\rm e} - r_{\rm e}^{\parallel}(ku_{{\rm e0}x}/\omega_{\rm ce})\sin\theta + i(2/\sqrt{\pi})(|k_{\parallel}|v_{\rm te}/\omega_{\rm ce})}\right], \tag{48}$$

$$A_{{\rm e}z} = \frac{E_{1z}}{B_0} + \frac{ku_{{\rm e0}x}}{\omega}\frac{E_{1x}\cos\theta - E_{1z}\sin\theta}{B_0}. \tag{49}$$

The x component of Eqn. 33 is

$$im_{\rm e}n_0\left(\omega-\mathbf{k}\cdot\mathbf{u}_{\rm e0}\right)u_{{\rm e}1x}=ik_\perp p_{\rm e1}^\perp+en_{\rm e0}(E_{1x}+B_0u_{{\rm e}1y}-u_{{\rm e}0z}B_{1y}). \tag{50}$$

With Eqns. 35, 34, and 47, $u_{{\rm e}1y}$ can be expressed as

$$\gamma_{{\rm e}y}u_{{\rm e}1y}=i\alpha_{{\rm e}x}u_{{\rm e}1x}-\frac{\sin\theta\cos\theta}{2\alpha_{\rm e}\alpha_{{\rm e}z}}\left(\frac{kv_{\rm te}^\perp}{\omega_{\rm ce}}\right)^2A_{{\rm e}z}-A_{{\rm e}x}, \tag{51}$$

where $\gamma_{{\rm e}y}$, $\alpha_{{\rm e}x}$, and $A_{{\rm e}x}$ are

$$\gamma_{{\rm e}y}=1+\frac{\sin\theta}{2\alpha_{\rm e}}\left(\frac{\epsilon}{k}\right)\left(\frac{kv_{\rm te}^\perp}{\omega_{\rm ce}}\right)^2\left[1+\frac{\cos^2\theta}{2\alpha_{\rm e}\alpha_{{\rm e}z}}\left(\frac{kv_{\rm te}^\parallel}{\omega_{\rm ce}}\right)^2\right], \tag{52}$$

$$\alpha_{{\rm e}x}=\alpha_{\rm e}-\frac{\sin^2\theta}{2\alpha_{\rm e}}\left(\frac{kv_{\rm te}^\perp}{\omega_{\rm ce}}\right)^2\left[1+\frac{\cos^2\theta}{2\alpha_{\rm e}\alpha_{{\rm e}z}}\left(\frac{kv_{\rm te}^\parallel}{\omega_{\rm ce}}\right)^2\right], \tag{53}$$

$$A_{{\rm e}x}=\frac{E_{1x}}{B_0}-\frac{ku_{{\rm e}0z}}{\omega}\frac{E_{1x}\cos\theta-E_{1z}\sin\theta}{B_0}. \tag{54}$$

The y component of Eqn. 33 is

$$im_{\rm e}n_{\rm e0}\left(\omega-\mathbf{k}\cdot\mathbf{u}_{\rm e0}\right)u_{1y}=en_{\rm e0}(E_{1y}-B_0u_{{\rm e}1x}-u_{{\rm e}0x}B_{1z}+u_{{\rm e}0z}B_{1x})+e(E_0-u_{{\rm e}0x}B_0)n_{\rm e1}. \tag{55}$$

With Eqns. 34, 29, and 47, $u_{{\rm e}1x}$ can be expressed as

$$\gamma_{{\rm e}x}u_{{\rm e}1x}=-i\alpha_{{\rm e}y}u_{{\rm e}1y}+\frac{i\cos\theta}{\alpha_{\rm e}\alpha_{{\rm e}z}}\frac{T_{\rm e0}^\perp}{T_{\rm e0}^\perp+T_{\rm i0}}\left(\frac{ku_{{\rm e}0x}}{\omega_{\rm ce}}\right)A_{{\rm e}z}+A_{{\rm e}y}, \tag{56}$$

where $\gamma_{{\rm e}x}$, $\alpha_{{\rm e}y}$, and $A_{{\rm e}y}$ are

$$\gamma_{{\rm e}x}=1+\frac{\sin\theta}{\alpha_{\rm e}}\frac{T_{\rm e0}^\perp}{T_{\rm e0}^\perp+T_{\rm i0}}\left(\frac{ku_{{\rm e}0x}}{\omega_{\rm ce}}\right)\left[1+\frac{\cos^2\theta}{2\alpha_{\rm e}\alpha_{{\rm e}z}}\left(\frac{kv_{\rm te}^\parallel}{\omega_{\rm ce}}\right)^2\right], \tag{57}$$

$$\alpha_{{\rm e}y}=\alpha_{\rm e}-\frac{1}{\alpha_{\rm e}}\left(\frac{\epsilon}{k}\right)\frac{T_{\rm e0}^\perp}{T_{\rm e0}^\perp+T_{\rm i0}}\left(\frac{ku_{{\rm e}0x}}{\omega_{\rm ce}}\right)\left[1+\frac{\cos^2\theta}{2\alpha_{\rm e}\alpha_{{\rm e}z}}\left(\frac{kv_{\rm te}^\parallel}{\omega_{\rm ce}}\right)^2\right], \tag{58}$$

$$A_{{\rm e}y}=\frac{E_{1y}}{B_0}-\frac{k}{\omega}\frac{(u_{{\rm e}0x}\sin\theta+u_{{\rm e}0z}\cos\theta)E_{1y}}{B_0}, \tag{59}$$

With Eqns. 51 and 56, $u_{{\rm e}1y}$ is given by

$$u_{{\rm e}1y}=i\left(iC_{yx}^{\rm e}A_{{\rm e}x}+C_{yy}^{\rm e}A_{{\rm e}y}+iC_{yz}^{\rm e}A_{{\rm e}z}\right), \tag{60}$$

where

$$C_{yx}^{\rm e}=\left(\gamma_{{\rm e}y}-\frac{\alpha_{{\rm e}x}\alpha_{{\rm e}y}}{\gamma_{{\rm e}x}}\right)^{-1}, \tag{61}$$

$$C_{yy}^{\rm e}=C_{yx}^{\rm e}\frac{\alpha_{{\rm e}x}}{\gamma_{{\rm e}x}}, \tag{62}$$

$$C_{yz}^{\rm e}=C_{yx}^{\rm e}\left[\frac{\sin\theta\cos\theta}{2\alpha_{\rm e}\alpha_{{\rm e}z}}\left(\frac{kv_{\rm te}^\perp}{\omega_{\rm ce}}\right)^2+\frac{\alpha_{{\rm e}x}\cos\theta}{\gamma_{{\rm e}x}\alpha_{\rm e}\alpha_{{\rm e}z}}\left(\frac{T_{\rm e0}^\perp}{T_{\rm e0}^\perp+T_{\rm i0}}\frac{ku_{{\rm e}0x}}{\omega_{\rm ce}}\right)\right]. \tag{63}$$

Similarly, $u_{{\rm e}1x}$ is given by

$$u_{{\rm e}1x}=iC_{xx}^{\rm e}A_{{\rm e}x}+C_{xy}^{\rm e}A_{{\rm e}y}+iC_{xz}^{\rm e}A_{{\rm e}z}, \tag{64}$$

where

$$C^{\mathrm{e}}_{xy} = \left(\gamma_{\mathrm{ex}} - \frac{\alpha_{\mathrm{ex}}\alpha_{\mathrm{ey}}}{\gamma_{\mathrm{ey}}}\right)^{-1}, \tag{65}$$

$$C^{\mathrm{e}}_{xx} = C^{\mathrm{e}}_{xy}\frac{\alpha_{\mathrm{ey}}}{\gamma_{\mathrm{ey}}}, \tag{66}$$

$$C^{\mathrm{e}}_{xz} = C^{\mathrm{e}}_{xy}\left[\frac{\cos\theta}{\alpha_{\mathrm{e}}\alpha_{\mathrm{ez}}}\left(\frac{T^{\perp}_{\mathrm{e0}}}{T^{\perp}_{\mathrm{e0}} + T_{\mathrm{i0}}}\frac{ku_{\mathrm{e0}x}}{\omega_{\mathrm{ce}}}\right) + \frac{\alpha_{\mathrm{ey}}\sin\theta\cos\theta}{2\gamma_{\mathrm{ey}}\alpha_s\alpha_{\mathrm{ez}}}\left(\frac{kv^{\perp}_{\mathrm{te}}}{\omega_{\mathrm{ce}}}\right)^2\right]. \tag{67}$$

Then, u_{s1z} can be written as

$$u_{\mathrm{e1}z} = iC^{\mathrm{e}}_{zx}A_{\mathrm{ex}} + C^{\mathrm{e}}_{zy}A_{\mathrm{ey}} + iC^{\mathrm{e}}_{zz}A_{\mathrm{ez}}, \tag{68}$$

where

$$C^{\mathrm{e}}_{zz} = -\frac{1}{\alpha_{\mathrm{ez}}} + \frac{\cos\theta}{2\alpha_{\mathrm{e}}\alpha_{\mathrm{ez}}}\left(\frac{kv^{\parallel}_{\mathrm{te}}}{\omega_{\mathrm{ce}}}\right)^2\left(C^{\mathrm{e}}_{xz}\sin\theta + C^{\mathrm{e}}_{yz}\frac{\epsilon}{k}\right), \tag{69}$$

$$C^{\mathrm{e}}_{zx} = \frac{\cos\theta}{2\alpha_{\mathrm{e}}\alpha_{\mathrm{ez}}}\left(\frac{kv^{\parallel}_{\mathrm{te}}}{\omega_{\mathrm{ce}}}\right)^2\left(C^{\mathrm{e}}_{xx}\sin\theta + C^{\mathrm{e}}_{yx}\frac{\epsilon}{k}\right), \tag{70}$$

$$C^{\mathrm{e}}_{zy} = \frac{\cos\theta}{2\alpha_{\mathrm{e}}\alpha_{\mathrm{ez}}}\left(\frac{kv^{\parallel}_{\mathrm{te}}}{\omega_{\mathrm{ce}}}\right)^2\left(C^{\mathrm{e}}_{xy}\sin\theta + C^{\mathrm{e}}_{yy}\frac{\epsilon}{k}\right). \tag{71}$$

The final goal is to obtain the perturbed current density of electrons, which is given by $\mathbf{J}^{\mathrm{e}}_1 = -en_{\mathrm{e0}}\mathbf{u}_{\mathrm{e1}} - e\mathbf{u}_{\mathrm{e0}}n_{\mathrm{e1}}$. Thus, an expression for n_{e1} is required. From Eqns. 34, 60, 64, and 68, n_{e1} is given by

$$n_{\mathrm{e1}} = \frac{kn_{\mathrm{e0}}}{\omega - \mathbf{k}\cdot\mathbf{u}_{\mathrm{e0}}}\left[iC'^{\mathrm{e}}_x A_{\mathrm{ex}} + C'^{\mathrm{e}}_y A_{\mathrm{ey}} + iC'^{\mathrm{e}}_z A_{\mathrm{ez}}\right], \tag{72}$$

where

$$C'^{\mathrm{e}}_x = C^{\mathrm{e}}_{xx}\sin\theta + C^{\mathrm{e}}_{yx}\epsilon/k + C^{\mathrm{e}}_{zx}\cos\theta, \tag{73}$$
$$C'^{\mathrm{e}}_y = C^{\mathrm{e}}_{xy}\sin\theta + C^{\mathrm{e}}_{yy}\epsilon/k + C^{\mathrm{e}}_{zy}\cos\theta, \tag{74}$$
$$C'^{\mathrm{e}}_z = C^{\mathrm{e}}_{xz}\sin\theta + C^{\mathrm{e}}_{yz}\epsilon/k + C^{\mathrm{e}}_{zz}\cos\theta. \tag{75}$$

Now we are ready for computing the dispersion relation. Eqn. 31 is

$$k^2_{\parallel}E_{1x} - k_{\perp}k_{\parallel}E_{1z} - i\omega\mu_0 J_{1x} = 0, \tag{76}$$
$$k^2 E_{1y} - i\omega\mu_0 J_{1y} = 0, \tag{77}$$
$$k^2_{\perp}E_{1z} - k_{\perp}k_{\parallel}E_{1x} - i\omega\mu_0 J_{1z} = 0. \tag{78}$$

By multiplying d_{i}^2, the above equation can be written as

$$K^2\cos^2\theta E_{1x} - K^2\sin\theta\cos\theta E_{1z} - i\Omega\frac{B_0}{en_0}J_{1x} = 0, \tag{79}$$
$$K^2 E_{1y} - i\Omega\frac{B_0}{en_0}J_{1y} = 0, \tag{80}$$
$$K^2\sin^2\theta E_{1z} - K^2\sin\theta\cos\theta E_{1x} - i\Omega\frac{B_0}{en_0}J_{1z} = 0, \tag{81}$$

where $K \equiv kd_{\mathrm{i}}$.

Eqns. 79–81 can be written as

$$\begin{pmatrix} D_{xx} & D_{xy} & D_{xz} \\ D_{yx} & D_{yy} & D_{yz} \\ D_{zx} & D_{zy} & D_{zz} \end{pmatrix}\begin{pmatrix} E_{1x} \\ E_{1y} \\ E_{1z} \end{pmatrix} = 0. \tag{82}$$

From Eqn. 32, each component of $i\Omega B_0 \mathbf{J}_{\mathrm{i1}}/en_0$ is

$$\frac{i\Omega B_0}{en_0} J_{i1x} = \zeta Z E_{1x} + \frac{\zeta Z'' \sin\theta}{2} \left(E_{1x} \sin\theta - i\frac{\epsilon}{k} E_{1y} + E_{1z} \cos\theta \right), \tag{83}$$

$$\frac{i\Omega B_0}{en_0} J_{i1y} = \zeta Z E_{1y}, \tag{84}$$

$$\frac{i\Omega B_0}{en_0} J_{i1z} = \zeta Z E_{1z} + \frac{\zeta Z'' \cos\theta}{2} \left(E_{1x} \sin\theta - i\frac{\epsilon}{k} E_{1y} + E_{1z} \cos\theta \right). \tag{85}$$

From Eqns. 64 and 72, $i\Omega J^{\mathrm{e}}_{1x}/en_0$ is given by

$$\frac{i\Omega B_0}{en_0} J^{\mathrm{e}}_{1x} = \Omega B_0 \left[\left(C^{\mathrm{e}}_{xx} + u_{\mathrm{e}0x} C^{\mathrm{e}}_k C'^{\mathrm{e}}_x \right) A_{\mathrm{e}x} - i \left(C^{\mathrm{e}}_{xy} + u_{\mathrm{e}0x} C^{\mathrm{e}}_k C'^{\mathrm{e}}_y \right) A_{\mathrm{e}y} + \left(C^{\mathrm{e}}_{xz} + u_{\mathrm{e}0x} C^{\mathrm{e}}_k C'^{\mathrm{e}}_z \right) A_{\mathrm{e}z} \right], \tag{86}$$

where $C^{\mathrm{e}}_k = K/(\Omega - \mathbf{K} \cdot \mathbf{u}_{\mathrm{e}0})$ and $\mathbf{u}_{\mathrm{e}0} = \mathbf{u}_{\mathrm{e}0}/V_{\mathrm{A}}$. Here $V_{\mathrm{A}} = B_0/\sqrt{\mu_0 m_{\mathrm{i}} n_0} = d_{\mathrm{i}}\omega_{\mathrm{ci}}$ is the Alfvén speed. Similarly, from Eqns. 68 and 72, $i\Omega J^{\mathrm{e}}_{1z}/en_0$ is given by

$$\frac{i\Omega B_0}{en_0} J^{\mathrm{e}}_{1z} = \Omega B_0 \left[\left(C^{\mathrm{e}}_{zx} + u_{\mathrm{e}0z} C^{\mathrm{e}}_k C'^{\mathrm{e}}_x \right) A_{\mathrm{e}x} - i \left(C^{\mathrm{e}}_{zy} + u_{\mathrm{e}0z} C^{\mathrm{e}}_k C'^{\mathrm{e}}_y \right) A_{\mathrm{e}y} + \left(C^{\mathrm{e}}_{zz} + u_{\mathrm{e}0z} C^{\mathrm{e}}_k C'^{\mathrm{e}}_z \right) A_{\mathrm{e}z} \right], \tag{87}$$

Since there is no y component in $\mathbf{u}_{\mathrm{e}0}$, $i\Omega J^{\mathrm{e}}_{1y}/en_0$ is simply

$$\frac{i\Omega B_0}{en_0} J^{\mathrm{e}}_{1y} = \Omega B_0 \left(iC^{\mathrm{e}}_{yx} A_{\mathrm{e}x} + C^{\mathrm{e}}_{yy} A_{\mathrm{e}y} + iC^{\mathrm{e}}_{yz} A_{\mathrm{e}z} \right). \tag{88}$$

In terms of dimensionless parameters, $\Omega B_0 A_{\mathrm{e}x}$, $\Omega B_0 A_{\mathrm{e}y}$, and $\Omega B_0 A_{\mathrm{e}z}$ can be written as

$$\Omega B_0 A_{\mathrm{e}x} = \left(\Omega - K u_{\mathrm{e}0z} \cos\theta \right) E_{1x} + (K u_{\mathrm{e}0z} \sin\theta) E_{1z}, \tag{89}$$

$$\Omega B_0 A_{\mathrm{e}y} = \left[K u_{\mathrm{e}0z} \cos\theta - K(u_{\mathrm{e}0x} \sin\theta + u_{\mathrm{e}0z} \cos\theta) \right] E_{1y}, \tag{90}$$

$$\Omega B_0 A_{\mathrm{e}z} = (K u_{\mathrm{e}0x} \cos\theta) E_{1x} + \left(\Omega - K u_{\mathrm{e}0x} \sin\theta \right) E_{1z}. \tag{91}$$

Then, each component of the tensor $\mathbf{D}$ is

$$\begin{aligned} D_{xx} =& K^2 \cos^2\theta - \zeta Z - \frac{\zeta Z''}{2} \sin^2\theta \\ & - \left[\left(C^{\mathrm{e}}_{xx} + u_{\mathrm{e}0x} C^{\mathrm{e}}_k C'^{\mathrm{e}}_x \right) \left(\Omega - K u_{\mathrm{e}0z} \cos\theta \right) + \left(C^{\mathrm{e}}_{xz} + u_{\mathrm{e}0x} C^{\mathrm{e}}_k C'^{\mathrm{e}}_z \right) K u_{\mathrm{e}0x} \cos\theta \right], \end{aligned} \tag{92}$$

$$D_{xy} = i \left(\frac{\epsilon}{k} \right) \frac{\zeta Z''}{2} \sin\theta + \left(C^{\mathrm{e}}_{xy} + u_{\mathrm{e}0x} C^{\mathrm{e}}_k C'^{\mathrm{e}}_y \right) \left[\Omega - K(u_{\mathrm{e}0x} \sin\theta + u_{\mathrm{e}0z} \cos\theta) \right], \tag{93}$$

$$\begin{aligned} D_{xz} =& - K^2 \sin\theta\cos\theta - \frac{\zeta Z''}{2} \sin\theta\cos\theta \\ & - \left[\left(C^{\mathrm{e}}_{xx} + u_{\mathrm{e}0x} C^{\mathrm{e}}_k C'^{\mathrm{e}}_x \right) K u_{\mathrm{e}0z} \sin\theta + \left(C^{\mathrm{e}}_{xz} + u_{\mathrm{e}0x} C^{\mathrm{e}}_k C'^{\mathrm{e}}_z \right) \left(\Omega - K u_{\mathrm{e}0x} \sin\theta \right) \right], \end{aligned} \tag{94}$$

$$D_{yx} = - i \left[C^{\mathrm{e}}_{yx} \left(\Omega - K u_{\mathrm{e}0z} \cos\theta \right) + C^{\mathrm{e}}_{yz} K u_{\mathrm{e}0x} \cos\theta \right], \tag{95}$$

$$D_{yy} = K^2 - \zeta Z - C^{\mathrm{e}}_{yy} \left[\Omega - K(u_{\mathrm{e}0x} \sin\theta + u_{\mathrm{e}0z} \cos\theta) \right], \tag{96}$$

$$D_{yz} = - i \left[C^{\mathrm{e}}_{yx} K u_{\mathrm{e}0z} \sin\theta + C^{\mathrm{e}}_{yz} \left(\Omega - K u_{\mathrm{e}0x} \sin\theta \right) \right], \tag{97}$$

$$\begin{aligned} D_{zx} =& - K^2 \sin\theta\cos\theta - \frac{\zeta Z''}{2} \sin\theta\cos\theta \\ & - \left[\left(C^{\mathrm{e}}_{zx} + u_{\mathrm{e}0z} C^{\mathrm{e}}_k C'^{\mathrm{e}}_x \right) \left(\Omega - K u_{\mathrm{e}0z} \cos\theta \right) + \left(C^{\mathrm{e}}_{zz} + u_{\mathrm{e}0z} C^{\mathrm{e}}_k C'^{\mathrm{e}}_z \right) K u_{\mathrm{e}0x} \cos\theta \right], \end{aligned} \tag{98}$$

$$D_{zy} = i \left(\frac{\epsilon}{k} \right) \frac{\zeta Z''}{2} \cos\theta + i \left(C^{\mathrm{e}}_{zy} + u_{\mathrm{e}0z} C^{\mathrm{e}}_k C'^{\mathrm{e}}_y \right) \left[\Omega - K(u_{\mathrm{e}0x} \sin\theta + u_{\mathrm{e}0z} \cos\theta) \right], \tag{99}$$

$$\begin{aligned} D_{zz} =& K^2 \sin^2\theta - \zeta Z - \frac{\zeta Z''}{2} \cos^2\theta \\ & - \left[\left(C^{\mathrm{e}}_{zx} + u_{\mathrm{e}0z} C^{\mathrm{e}}_k C'^{\mathrm{e}}_x \right) K u_{\mathrm{e}0z} \sin\theta + \left(C^{\mathrm{e}}_{zz} + u_{\mathrm{e}0z} C^{\mathrm{e}}_k C'^{\mathrm{e}}_z \right) \left(\Omega - K u_{\mathrm{e}0x} \sin\theta \right) \right]. \end{aligned} \tag{100}$$

Required input plasma parameters for the dispersion relation include B_0, n_0, $T^{\|}_{\mathrm{e}0}$, $T^{\perp}_{\mathrm{e}0}$, $T_{\mathrm{i}0}$, and $\mathbf{u}_{\mathrm{e}0}$. For $\mathbf{u}_{\mathrm{e}0}$, the coordinate transform from the LMN to local xyz coordinate system is needed. The z direction is along $\mathbf{B}_0$ and the y direction is along $\mathbf{B}_0\times$

$\mathbf{u}_{e0}$. The choice of the gradient (y) direction is based on the model geometry where there is no y component of $\mathbf{u}_{e0}$, and based on the MHD equilibrium, $\nabla p = \mathbf{B}\times\mathbf{J}$, which also indicates no y component of $\mathbf{u}_{e0}$.

References

Ji, H., Kulsrud, R., Fox, W., & Yamada, M. (2005). An obliquely propagating electromagnetic drift instability in the lower hybrid frequency range. *J. Geophys. Res.*, *110*, A08212.

Ji, J.-Y., & Held, E. D. (2008). Landau collision operators and general moment equations for an electron-ion plasma. *Physics of Plasmas*, *15*(10), 102101. Retrieved from `https://doi.org/10.1063/1.2977983` doi: 10.1063/1.2977983

Ji, J.-Y., & Joseph, I. (2018). Electron parallel closures for the 3 + 1 fluid model. *Phys. Plasmas*, *25*(3), 032117. Retrieved from `https://doi.org/10.1063/1.5014996` doi: 10.1063/1.5014996